ABSTRACT

An Investigation of Electrostatic Properties of Dust Grains in a Complex Plasma

Razieh Yousefi, Ph.D.

Advisor: Lorin Swint Matthews, Ph.D.

Explanation of the electrostatic behavior of dust grains in complex plasmas requires a knowledge of their basic properties such as electrostatic charge and dipole moment. While the measurement of the charge on symmetric dust grains in laboratory experiments has been performed, dust grains in astrophysical and laboratory plasmas are not necessarily spherically symmetric: the grains are typically elongated or aggregates consisting of many small subunits. Many of the previous works on grain charge assume a uniform plasma condition, though in the sheath of the rf discharge, there is an ion flow toward the boundary of the plasma. In this study, we present models for these complex plasma environments, where dust aggregates and dust structures formed in a laboratory plasma. Their basic properties are investigated experimentally and by employing computer models examining 3D structures of aggregates under different plasma conditions. The results support the previous experimental and numerical predictions for aggregates in these environments.

An Investigation of Electrostatic Properties of Dust Grains in a Complex Plasma

by

Razieh Yousefi, B.Sc., M.Sc.

A Dissertation

Approved by the Department of Physics

Dwight Russell, Ph.D., Chairperson

Submitted to the Graduate Faculty of
Baylor University in Partial Fulfillment of the
Requirements for the Degree
of
Doctor of Philosophy

Approved by the Dissertation Committee

Lorin Swint Matthews, Ph.D., Chairperson

Truell W. Hyde, Ph.D.

Gerald B. Cleaver, Ph.D.

Qin Sheng, Ph.D.

Anzhong Wang, Ph.D.

Accepted by the Graduate School
December 2015

J. Larry Lyon, Ph.D., Dean

Page bearing signatures is kept on file in the Graduate School.

TABLE OF CONTENTS

LIST OF FIGURES

LIST OF TABLES

ACKNOWLEDGMENTS

I would like to express my deepest gratitude to my mentor, Dr. Lorin Matthews, and co-mentor, Dr. Truell Hyde, for their excellent guidance, caring, patience, providing me with an excellent atmosphere for doing research, and supporting me financially through the National Science Foundation under Grant No. 0847127 and 1262031. I would like to thank Dr. Wang, who let me experience the research in theoretical physics.

I would like to thank Dr. Jie kong, Dr. Ke Qiao, and Jorge Carmona Reyes for always being willing to help providing and interpreting data, explaining concepts, and providing moral support. I would like to thank Dr. Rene Laufer, especially for his excellent tour guiding to NASA Space Center. Many thanks to Mudi Chen and Michael Dropmann, who as good friends, were always willing to help and give their best suggestions. It would have been a lonely research lab without them. Thanks to my friends Meera Gurung, Aditi Mukhopadhyay, Karen Bland Low, and Chava Baker who always had time to listen and laugh.

I would also like to thank my parents who always supported me, encouraged me, and stood by me. Many thanks to my sisters and brothers for their support with their best wishes. Finally, I would like to thank my husband, Ahmad Borzou, who was always willing to help, cheering me up, and who stood by me through the good times and bad.

To my always encouraging and ever faithful parents, Ehsan and Afrooz Yousefi

CHAPTER ONE

Introduction

As energy is applied to matter, its state transforms in the sequence solid, liquid, gas, and ionized gas or plasma. In order to ionize a gas, sufficient energy is provided to free electrons from their parent gas molecules in order to produce ions, resulting in overall neutral matter, though the motion of the two species can generate electric currents and magnetic fields.

The energy required to ionize a plasma can be supplied by heat or strong electromagnetic fields. The charged species in the plasma respond to the electromagnetic fields, but in turn this results in altering the electric and magnetic fields. These characteristics make plasma the most challenging state of matter to model and understand due to the non-linear nature of the related physics [1].

1.1 Historical Background

The history of the study of plasmas is quite old [2]. A bright comet observed by our distant ancestors is an excellent example of the cosmic laboratory for the study of plasma, while flames are one of the most familiar plasmas encountered on earth. It is amazing that the ancients thought of fire as a fourth state of matter (other than earth, water and air), while we gave this designation to a plasma only about 85 years ago.

Man-made plasma was first discovered by English physicist William Crookes in the 1870s through the invention of the electrical discharge tube. A Crookes tube consists of a partially evacuated glass container with metal electrodes at each end. When a high voltage is applied across the electrodes, “cathode rays” are sustained through the gas, so named since they are emitted by the cathode. At the time, the properties of the cathode ray were unknown. The debate about their source continued until

J. J. Thompson identified cathode rays as negatively charged particles, later named electrons. When a high voltage is applied across an evacuated tube, electrons are released from the cathode and accelerated, traveling in a straight line. While cathode rays themselves are invisible, as they strike atoms in the wall opposite the cathode, they cause the walls to fluoresce. Any residual gas in the tube can also be seen to glow as the high energy electrons transfer energy to the gas molecules, exciting electrons which emit photons as they recombine with the ions.

The term "plasma" was first used by Langmuir (1928), the Nobel prize-winning American chemist, to describe the inner region of a glowing ionized gas produced by means of an electric discharge in a tube [3, 4]. Langmuir was a researcher at General Electric working on electric devices based on ionized gasses, and the manner in which the high velocity charged particles were carried through electrified fluid. Langmuir's research became the theoretical basis of most plasma processing techniques in use today.

In the middle of the 19th century, Broun anticipated the nature and origin of the solar wind, solar magnetic fields, sunspot activity and geomagnetic storms [5, 6]. For the first time he applied the experimental results of the behavior of ionized gases in discharge tubes to space physics, which may be considered as the beginning of astrophysical plasma physics. The experimental confirmation of Broun's hypotheses become possible only during the second half of 20th century and the advent of the space age with the discovery of the Van Allen radiation belts, layers of energetic charged particles surrounding the earth held in place by the planet's magnetic field [7].

1.2 Dusty Plasma

Dusty plasmas, ubiquitous in cosmic plasmas, planetary plasmas, plasmas near the earth and plasmas in the laboratory, are also known as colloidal or complex plasmas. Dusty plasmas contain macroscopic solid particles immersed in a plasma environment of electrons, ions and neutral gas molecules. Dust grains are massive compared to the plasma species (billions times heavier than the protons) and their sizes range from nanometres to millimetres [8]. They may be metallic and conducting, silicates, or made of fluffy ice crystals or even liquid droplets and their shapes are irregular, unless they are man-made [9]. The dust may be in the shape of spheres, rods, irregularly shaped pancakes, or agglomerates of these shapes.

Dust particles are generally charged by collecting electrons and ions and thus act as an additional plasma species. The name "complex plasmas" refers to the complexity of studying dusty plasmas; however, they are interesting because the presence of dust affects the charged particles' equilibrium, especially when the number density of dust is large. The surface electric potential of dust particles is typically 1-10 V (positive or negative). The potential is usually negative because the electrons are more mobile than the ions, thus they collide with the dust more frequently and resulting in a net negative charge.

Dust particles may accrete into larger particles, usually referred to as "grain plasmas" or dust aggregates. This phenomena takes place in astrophysical environments, such as nebulae and interstellar and protoplanetary disks as well as in laboratory dusty plasmas where the dynamics of the charged dust grains are directly observable. In the lab, dusty plasmas forming liquid or crystalline states and dust crystals, which have a varied structures and sizes, are observable under laser illumination with the naked eyes. The motion of individual dust grains can be easily imaged with a camera equipped with a microscope lens. A representative example of dust crystal is shown in Figure 1.1.

1.3 Space Dusty Plasmas

About 99.999% of the visible matter in the universe is in the plasma state. In many environments, the plasma contains solid particles, forming a dusty plasma [10, 11]. For instance, interstellar clouds, the space between the stars (shown in Fig. 1.2), is

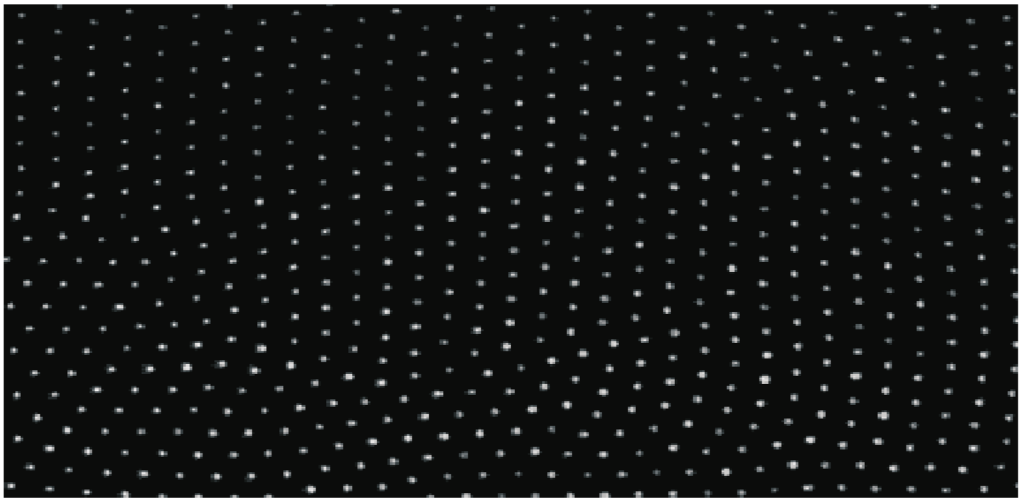

Figure 1.1: A two dimensional crystal structure formed in the laboratory dusty plasma (Courtesy of http://www.mpe.mpg.de/pke/index.html).

(a)

(b)

Figure 1.2: Examples of cosmic dusty plasmas. (a) Interstellar space: the clouds of gas and dust between the stars are visible at infrared wavelengths (Courtesy of NASA/Jet Propulsion Laboratory (JPL)). (b) Comets: nucleus, coma and tail (Courtesy of NASA/JPL).

Figure 1.3. Artist's impression of a protostellar disk (Courtesy of NASA/JPL).

filled with ionized gas and dust particles [12]. A protostellar disk is a rotating disk of gas and dust surrounding a young, newly formed star which forms when a gas cloud collapses and becomes hot enough to ignite the star at the center (Fig. 1.3).

Our solar system is also full of dust [13] with plasma generated from solar outflows. Comets are small bodies with irregular shapes composed of an admixture of non-volatile grains and frozen gases. As comets approach the Sun, they heat up partially and develop a large cloud composed of diffuse material, called a coma, consisting of ionized gas and dust (Fig. 1.2(b)) [14, 15]. Interplanetary space is filled by "interplanetary dust" (Fig. 1.4(a)) which generally originates from the decay by collision fragmentation of debris from comets [16] and asteroids, which produce dust during mutual collisions in the asteroid belt. Planetary rings, the ring systems around planets, are also made of micron- to submicron-sized dust particles (Fig. 1.4(b)). Though larger rocks and boulders are present in several of Saturn's rings, many of the rings as well as those around Jupiter, Uranus, and Neptune are composed of dust. The composition of ring particles varies: they may be composed of silicates or ices [17, 18, 19].

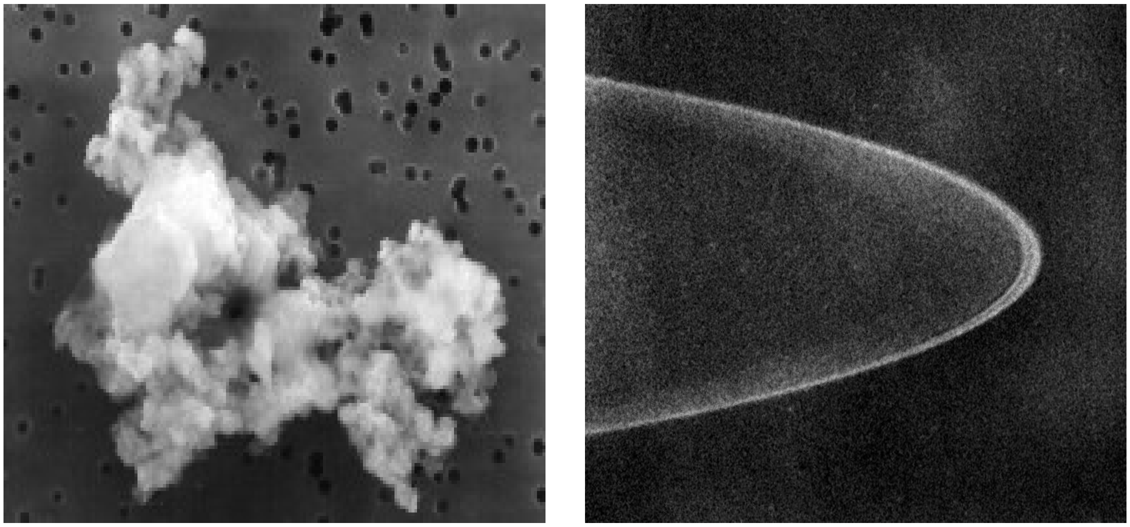

(a) (b)

Figure 1.4: Example of dusty plasma in the solar system. (a) Interplanetary dust collected in the stratosphere with a U2 aircraft. (Courtesy of NASA/JPL). (b) Planetary ring: Ring of Jupiter made of dust particles with 0.1-10 μm particle sizes to large bodies with 1 cm to 0.5 km size (Courtesy of NASA/JPL).

The radial extent of the ring may vary from a few km to a few hundred of thousands km, with a number density of dust in the rings varying from $10^{-}8(cm^{-3})$ to $10(cm^{-3})$.

One interesting feature of the Earth's environment is "noctilucent clouds", also known as "night shining" clouds, a special type of cloud formed in the polar summer mesopause (Fig. 1.5). Noctilucent clouds are the highest clouds in Earth's atmosphere and composed of tiny crystals of water ice, requiring water vapour, dust, and very cold temperatures to form. The sources of both the dust and the water vapor in the upper atmosphere are not known with certainty. Some claim that these clouds were not observed before 1885, and they could be a result of increased dust in the upper atmosphere due to environmental change, especially the explosion of the Krakatoa volcano in 1883 [20].

1.4 Laboratory Dusty Plasmas

In order to understand dusty plasmas in space, low-pressure laboratory dusty plasmas are used as a model since they share the same basic physics. Charged dust

Figure 1.5. Noctilucent clouds over Finland (Courtesy of National Geographic).

particles are contained within a plasma chamber, with their dynamics controlled by electromagnetic and gravitational forces. Thus, many conditions differ such as geometric boundaries within the structure, composition of the dust, temperature, and conductivity [8], as well as spatiotemporally varying boundary conditions which are imposed by the external circuit, the mechanism which is used to sustain the plasma [12].

The majority of devices in which dusty plasmas can be produced are direct current (dc) and radio-frequency (RF) discharges, plasma processing reactors, and fusion plasma devices. Among these, the most popular laboratory dusty plasmas are RF and dc discharges in which the gas is ionized by passing an electric current through the gas medium.

The dc glow discharge has been historically important for studying the properties of the plasma medium as well as applications of weakly ionized plasmas. This system, first made by William Crookes and known as the Crookes tube, is created by applying

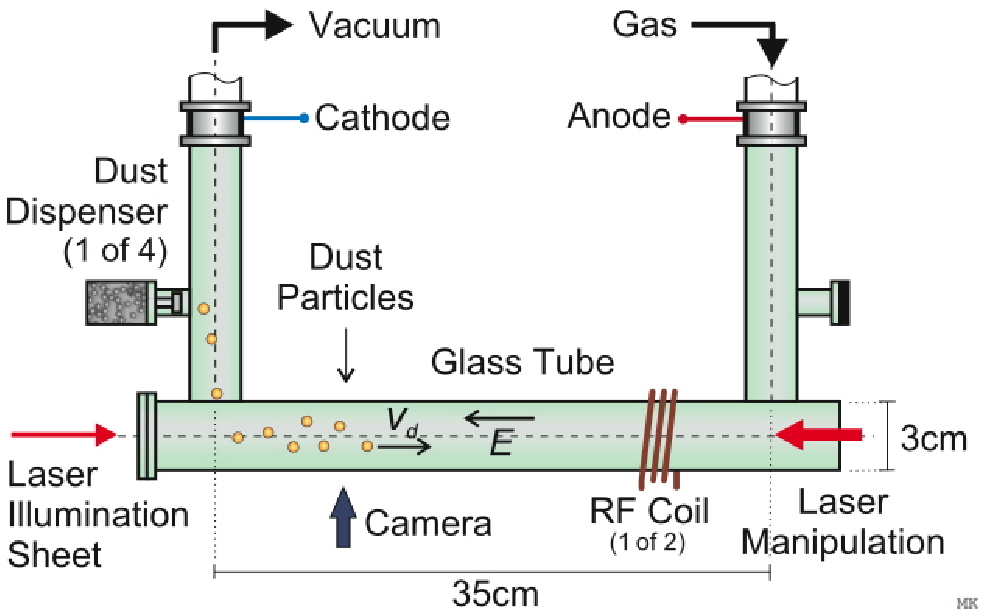

Figure 1.6: Illustration of dc discharge representing its most important parameters (Courtesy of PK-4 Webmaster).

a voltage between two metal electrodes in a glass tube containing gas at low pressure. Before application of the potential, gas molecules are electrically neutral, though the gas will contain a very small number of charged particles due to a free electron occasionally being released from a gas molecule by the random high energy collision with another gas molecule, for example. When a large voltage is applied between the electrodes, all the free electrons which may be present are rapidly accelerated toward the anode. Because of their comparably small mass, they attain a high velocity (kinetic energy) and collide with gas molecules and ionize them, forming a plasma, and begin conducting electricity. The recombination of electrons and ions causes it to glow; the color of the light emitted depends on the gas used. By analyzing the light produced by spectroscopy, information about the atomic interactions in the gas can be derived. As a result, glow discharges are used in plasma physics as well as analytical chemistry.

An apparatus similar to a Crookes tube is the most common configuration of a dc discharge, which has the advantage of symmetry [21]. Fig. 1.6 illustrates a

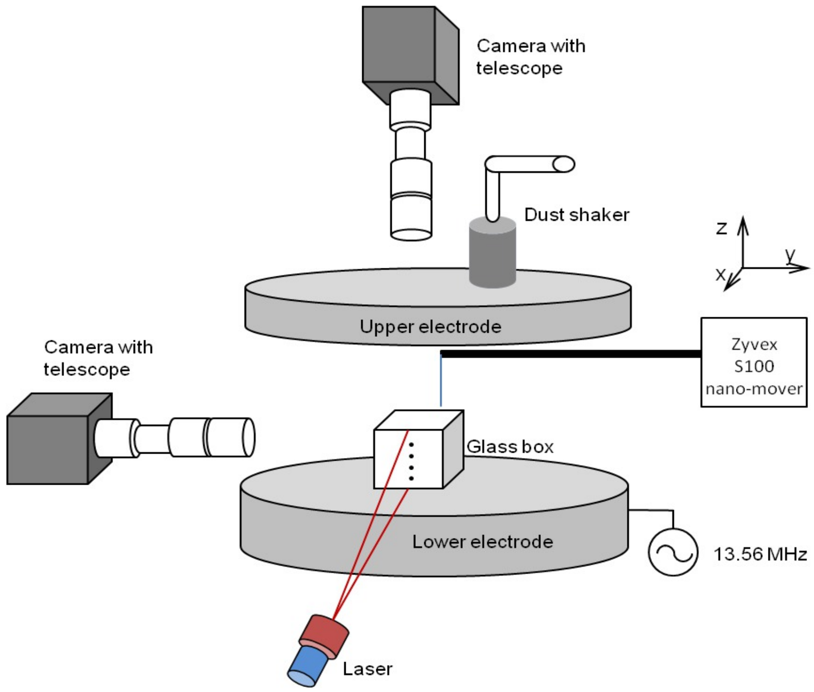

Figure 1.7: Illustration of a typical RF discharge setup used in research laboratories (Courtesy of CASPER, Baylor).

dc discharge tube which shows that a dc chamber allows great optical access for diagnostics as well as laser manipulation.

Another typical low-pressure discharge which is used in laboratories is a radio-frequency (RF) discharge maintained by RF currents and voltages. Generally, an RF discharge consists of two parallel electrodes with RF voltage applied directly to one of the electrodes, while the other one is grounded. The usual operating frequencies range from 40 kHz to 40MHz with the most common frequency 13.56 MHz for typical plasma processing application in the laboratories. The RF discharge is a very efficient trap for macroscopic, negatively charged dust particles because of its strongly inhomogeneous vertical and horizontal electric fields.

Fig. 1.7 shows a typical setup for a RF discharge which is composed of two parallel plates (lower and upper electrodes) creating a sinusoidal current applied across a discharge between the parallel electrodes. In this setup the upper electrode is a hollow cylinder in order to allow optical access. A gas with neutral density n_g is present between the plates, partially ionized and form the plasma between the plates. In order to provide a confinement for dust particles levitated in the lower sheath of the plasma, a glass box is placed on the lower electrode.

1.5 Motivation

In order to better understand and explain a dusty plasma, a knowledge of the basic properties of the dust particles is required. In a dusty plasma the dust is charged, either by being immersed in a radiative or plasma environment or through triboelectric charging. The particle electrostatic charge and dipole moment are two of the most important parameters which help determine the dusty plasma dynamics since they determine both the particle interactions with themselves as well as with the plasma particles and existing electromagnetic fields.

Most previous works assume a symmetric geometry for the dust, such as a sphere or cylinder, while aggregate structure is a common form among cosmic dust. Due to their porous, complex structure, the charging of aggregates may differ significantly from that of symmetric particles. In addition, complex structures consisting of multiple particles, such as a one-dimensional crystalline structure, makes it hard to quantify the charge distribution on the dust particles. In the current study, the electrostatic properties of dust aggregates as well as multiple-particle structures are investigated both numerically and experimentally and the results are compared to previous work.

1.6 Dissertation Layout

In this dissertation, the basic charge characteristics of dust aggregates immersed in plasma are investigated using different experimental and numerical methods. These include the electrostatic charge and dipole moment, as well as the external electric field surrounding the dust. Chapter Two discusses the fundamental properties of a dusty plasma and provides theoretical studies of charging of the dust in a homogeneous and isotropic dusty plasma as well as a flowing plasma. Chapter Three is devoted to the theory governing dynamics of the dust by examining different forces and torques acting on the dust grain in a dusty plasma. In Chapter Four, the electric charges and dipole moments of aggregates are found by observing the dynamics of aggregates formed in the lab and compared to those predicted by computer models. In Chapter Five, the dynamics of particles in a vertical dust chain are examined numerically to determine charges on individual dust grains, which can be used to probe local plasma conditions. Chapter Six provides a numerical investigation of charging of dust aggregates in the presence of ion flow. Chapter Seven summarizes the results.

CHAPTER TWO

Physics of Dusty Plasma

A plasma with dust particles or grains is termed as a dusty plasma. Dusty plasmas have a number of physical properties including charge neutrality and Debye shielding. However, in studies of dusty plasma behavior, the central point is to understand the charging of a dust grain immersed in the plasma. An understanding of the fundamental properties and charging processes of dust particles help us to investigate the dynamics of a dusty plasma. In this chapter we present a brief description of fundamental characteristics of a dusty plasma along with different charging mechanisms which lead us to study the dynamics of dust in a complex plasma.

2.1 Charge Neutrality

When there are no external disturbance on a dusty plasma, the net electric charge is zero. The charge neutrality condition in a dusty plasma is given by

$$q_e n_{0e} \; + \; Q_d n_{0d} \; + \; q_i n_{0i} \; = \; 0 \tag{2.1}$$

where $q_{e/i}$ is the electron (ion) charge $(e/-e)$, $n_{0e/i}$ is the number density of electrons (ions), Q_d is the dust particle charge, and n_{0d} is the number density of dust grains. In general, for singly ionized plasmas, n_{0e} and n_{0i} are taken to be equal; however, in laboratory and space dusty plasmas with large dust densities, significant depletion of the electron number density may occur since a large fraction of the background electrons may be bound to the dust surface or other solid boundaries in the plasma environment [12].

2.2 Debye Sheath

Since plasma is a conducting fluid, the ability of the plasma to shield the electric field of an individual charged dust particle, or any solid surface in a plasma with a non-zero potential, is another fundamental characteristic of a plasma. In the following sections we will present the shielding length derived for dust particles immersed in plasma as well as the sheaths developed in front of solid boundaries.

2.2.1 Dust Particle Debye Sheath

A dust particle placed inside the plasma attracts particles of opposite charge and repels particles of the same charge, forming a cloud surrounding the dust particle, referred to as the sheath. The thickness of the sheath can be approximately calculated. We assume that in a uniform plasma the electric potential at the surface of the dust ($r = a$) is ϕ_s and also dust particles are massive compared to the ions, $m_d \gg m_i$, so that the dust particles' motion is not significant as a result of their large inertia. The electrons and ions are also assumed to be in local thermodynamic equilibrium with their number density given by the Boltzmann distribution, namely [22]

$$n_e = n_{0e} \exp(\frac{e\phi_s}{k_B T_e}) \tag{2.2}$$

and

$$n_i = n_{0i} \exp(-\frac{e\phi_s}{k_B T_i}) \tag{2.3}$$

where n_{0e} and n_{0i} are the electron and ion number densities far away from the cloud. Poisson's equation for this plasma condition is

$$\nabla^2 \phi_s = 4\pi(en_e - en_i - q_d n_d). \tag{2.4}$$

According to our assumption, the dust particle number density inside and outside of the sheath is the same, $q_d n_d = q_d n_{0d} = en_{0e} - en_{0i}$. Assuming $e\phi_s/k_B T_e \ll 1$ and $e\phi_s/k_B T_i \ll 1$, substituting Eqs. 2.2 and 2.3 into Eq. 2.4, we have

$$\nabla^2\phi_s = (\frac{1}{\lambda_{De}^2} + \frac{1}{\lambda_{Di}^2})\phi_s \tag{2.5}$$

where λ_{De}^2 and λ_{Di}^2 are the electron and ion shielding lengths respectively, and given as

$$\lambda_{De} = (k_B T_e / 4\pi n_{0e} e^2)^{1/2} \tag{2.6}$$

and

$$\lambda_{Di} = (k_B T_i / 4\pi n_{0i} e^2)^{1/2} \tag{2.7}$$

respectively, in which k_B is the Boltzmann constant, and $T_{e/i}$ is the plasma electron/ion temperature. By assuming $\phi_s = \phi_{0s}\exp(-r/\lambda_D)$, from Eq. 2.5 the total Debye length, which is a combination of the electron and ion shielding is given by

$$\lambda_D = \frac{\lambda_{De}\lambda_{Di}}{\sqrt{\lambda_{De}^2 + \lambda_{Di}^2}} \tag{2.8}$$

The thickness of the sheath, λ_D, is the measure of the shielding distance, the distance over which a charged particle inside the plasma feels the influence of the electric field of another individual charged particle [23].

In laboratory RF plasmas, $T_e \gg T_i$. comparing Eqs. 2.6 and 2.7 one can see that $\lambda_{De} \gg \lambda_{Di}$ and accordingly $\lambda_D \cong \lambda_{Di}$. This means that the shielding distance is mainly determined by the ion temperature and number density but the exact nature of the shielding in the sheath is an open question. However, when $T_e \ll T_i$, we have $\lambda_{De} \ll \lambda_{Di}$ and corresponds to $\lambda_D \cong \lambda_{De}$.

2.2.2 Debye Sheaths and Surfaces

In all laboratory plasma devices the plasma is confined between finite solid boundaries (walls). The thin layer between the boundary surface and the bulk plasma is known as the plasma sheath. The width of this layer may reach several tens of Debye lengths and in general depends on the plasma parameters such as temperature and density.

Since electrons are much more mobile than ions, they collide more often with the material surface, charging it negatively compared to the plasma bulk. There is always a persistent ion flow toward the wall through the plasma sheath. Consequently, the sheath has a greater density of ions compared to that of the electrons.

As shown in Fig. 2.1, at the plasma-sheath interface ($x = 0$) the electric potential of the plasma, Φ, is defined to be zero and $n_e(0) = n_i(0)$. Ions are assumed to enter the sheath with a velocity v_s. Throughout the sheath region, ion energy conservation requires [21]

$$\frac{1}{2}m_i v^2(x) = \frac{1}{2}m_i v_s^2 - e\Phi(x) \tag{2.9}$$

The continuity of ion flux is given by

$$n_i(x)v(x) = n_{i0}v_s \tag{2.10}$$

where n_{i0} is the ion density at the sheath edge. From Eqs. (2.9) and (2.10) we have

$$n_i = n_{i0}(1 - \frac{2e\Phi}{m_i v_s^2})^{1/2} \tag{2.11}$$

Thus as the potential is increasingly negative towards the boundary surface, the ion density increases. From the Boltzmann relation, the electron density is given by

$$n_e(x) = n_{es}\exp(\frac{\Phi(x)}{T_e}). \tag{2.12}$$

Setting $n_{es} = n_{i0} = n_s$ at the sheath edge and substituting Eqs. (2.11) and (2.12) into Poisson's equation

$$\frac{d^2\Phi}{dx^2} = \frac{e}{\epsilon_0}(n_e - n_i) \tag{2.13}$$

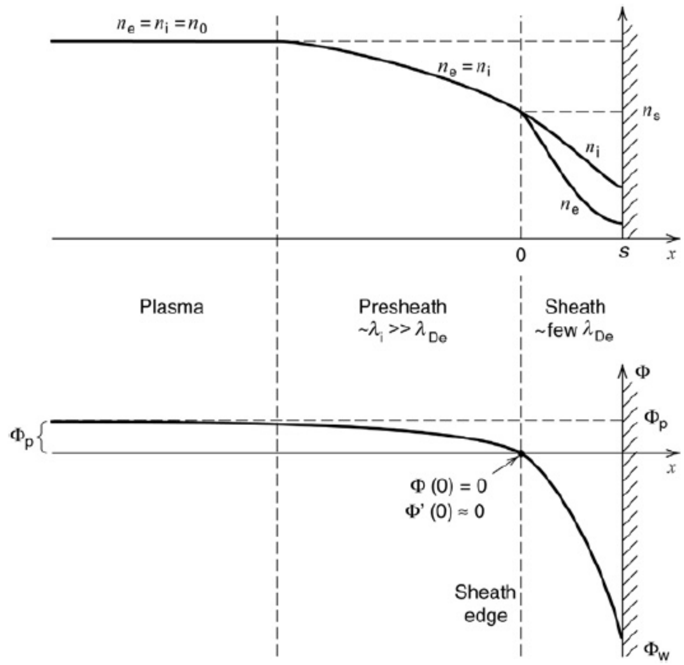

Figure 2.1: A qualitative characteristic of sheath and presheath at the interface of plasma with a solid boundary. Figure adapted from [21].

we derive

$$\frac{d^2\Phi}{dx^2} = \frac{en_s}{\epsilon_0}[exp\frac{\Phi}{T_e} - (1 - \frac{\Phi}{\xi_s})^{-1/2}] \tag{2.14}$$

where $e\xi_s = \frac{1}{2}m_i v_s^2$ is the initial energy of the ion. Eq. (2.32) has a stable solution only if v_s is sufficiently large,

$$v_s \geq v_B = (\frac{eT_e}{m_i})^{1/2} \tag{2.15}$$

where v_B is the Bohm velocity [21]. This result is known as Bohm sheath criterion. In order to provide a sufficiently large ion velocity, a transition layer or presheath must exist between the neutral plasma and the sheath. This region is not strictly field free, although the electric field is very small there.

2.3 Charging of Isolated Dust Grains

Charging of the dust particles plays a very important role in understanding the physics of dusty plasmas. The dominant elementary processes which lead to the charging of the dust particles are complex and depend on many environmental parameters. These mainly include dust particle interaction with the plasma particles, electrons and ions, as well as dust particle interaction with photons.

When a dust grain is immersed in a plasma, it collects plasma particles, electrons and ions, and becomes charged. Some of the plasma particles may be very energetic, and as they hit the surface of the dust, they are either reflected or pass through the dust. In this process, the energetic plasma particles may lose some of their energy by exciting other electrons within the dust grains and releasing them from the surface. These emitted electrons are called secondary electrons. The absorption of energy from high energy photons incident on the surface of the dust may also excite electrons and cause photoemission of electrons. This process, as well as secondary electron emission, tends to make the particle charge positively. Note that in our experiments, we have low temperature plasma with no UV photons, so the charging is due to the primary electron and ion currents.

2.3.1 Collection of Plasma Particles: Orbital Motion Limited (OML) Theory

A dust particle immersed in a plasma collects the ions and electrons that hit the surface of the dust. Since electrons have a greater thermal velocity, they collide with the surface more often. As a result, the surface electric potential of the dust tends to become negative. The flow of ions and electrons to the surface is highly affected by the dust surface potential; a negatively charged particle absorbs more ions and repels more electrons. The same argument can be applied to a positively charged dust particle.

A dust particle can be considered as a small probe, allowing the prediction of the electron and ion currents to the probe in the form of a theoretical model known as orbital motion limit (OML) theory, first derived by Mott-Smith and Langmuir in 1926 [24]. In this model it is assumed that electrons and ions originate from infinity and move towards the dust particle on collisionless orbits subject only to the electrostatic interaction with the dust particle. This requires the condition $r_d \ll \lambda_D \ll \lambda_{mfp}$ to be valid, in which r_d is the dust radius, λ_D is the Debye length of the dust particle, and λ_{mfp} is the collisional mean-free-path between neutral gas atoms and either electrons or ions [25, 26]. It is also assumed that the surface of the dust is an equipotential surface.

In the following we calculate the plasma currents to the surface of the dust based on the above assumptions [23, 27, 28]. We assume that a plasma particle's velocity before and after a collision with the surface of the dust are v_j and v_{jf} respectively. The charging collision cross section is $\sigma_j^D = \pi b_j^2$ with b_j as the impact factor (Fig. 2.2). The equations for conservation of momentum and energy are given by

$$m_j v_j b_j = m_j v_{jf} r_d \tag{2.16}$$

and

$$\frac{1}{2} m_j v_j^2 = \frac{1}{2} m_j v_{jf}^2 + \frac{1}{4\pi\epsilon_0} \frac{q_j q_d}{r_d} \tag{2.17}$$

The surface potential ϕ_s and the capacitance C of the dust are related to the charge of the dust through $C = q_d/\phi_s$. The capacitance of a spherical dust grain in a plasma is $C = r_d \exp(-r_d/\lambda_D) \simeq r_d$ for $\lambda_D \gg r_d$. This easily implies that $q_d = r_d\phi_s$. Using this relation along with Eqs. 2.16 and 2.17, the collision cross relation, σ_j^d, becomes

$$\sigma_j^d = \pi r_d^2 (1 - \frac{2 q_j \phi_s}{m_j v_j^2}) \tag{2.18}$$

Thus the cross section is increased if the charge of the dust and the plasma species are opposite. The plasma particle current, carried by the plasma particle species j, to the surface of the dust is

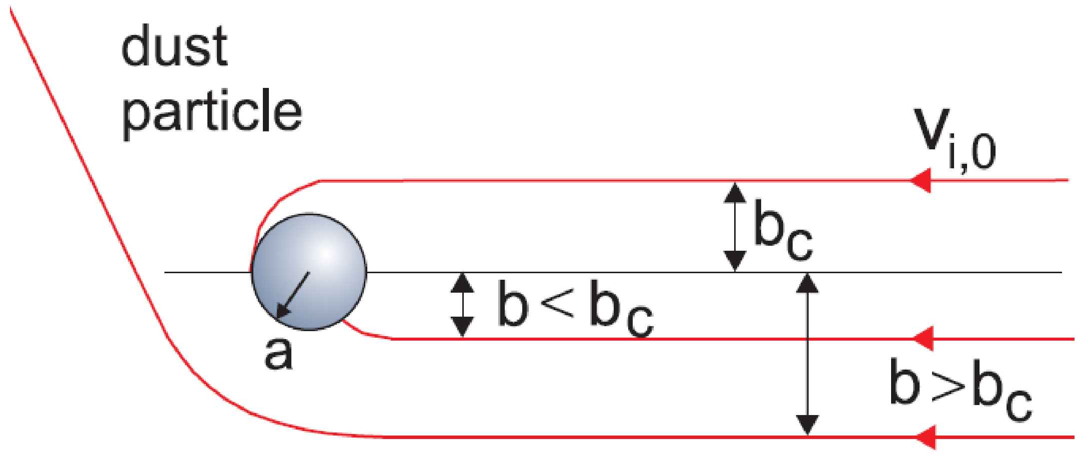

Figure 2.2: Ion trajectories for different impact factors b. As shown in the figure, for impact factors less than or equal to the critical impact factor, b_c, ions collide with the surface of the dust particle, while those with an impact factor greater than b_c will only be deflected by the electric field of the dust. Figure adapted from [29]

$$I_j = q_j n_j \int_{v_j^{min}}^{\infty} v_j \sigma_j^D f_j(v_j) d\mathbf{v}_j^3 \tag{2.19}$$

where n_j is the number density of plasma species j with velocity distribution $f_j(v_j)$ given by

$$f_j(v_j) = (\frac{m_j}{2\pi k_B T_j})^{3/2} \exp(-\frac{m_j \mathbf{v_j}^2}{2k_B T_j} - \frac{q_j \phi_s}{k_B T_j}). \tag{2.20}$$

In the limits of the integral, v_j^{min} is the minimum value of the velocity of a plasma particle which is able to collide with the surface of the dust. When the plasma particle charge is opposite the surface potential, $q_j \phi_s < 0$, v_j can take any value and $v_j^{min} = 0$. On the other hand, if $q_j \phi_s > 0$, the plasma particle and dust grain repel each other, so the plasma particle must be energetic enough to overcome this repulsion. In other words, the plasma particle energy should be greater than or equal to zero at the collision point, and conservation of energy yields the result that

$$v_j^{min} = (-\frac{2q_j\phi_s}{m_j})^{1/2} \tag{2.21}$$

Using Eqns. 2.18, 2.20, and 2.21 in Eq. 2.19 and performing the integral in spherical polar coordinates I_j is found to be [24, 28, 30]

$$I_j = 4\pi r_d^2 n_j q_j (\frac{k_B T_j}{2\pi m_j})^{1/2}(1 - \frac{q_j\phi_s}{k_B T_j}) \qquad q_j\phi_s < 0 \tag{2.22}$$

and

$$I_j = 4\pi r_d^2 n_j q_j (\frac{k_B T_j}{2\pi m_j})^{1/2}\exp(\frac{q_j\phi_s}{k_B T_j}) \qquad q_j\phi_s > 0 \tag{2.23}$$

These derivations are based on the assumption of collisionless ion trajectories for any Maxwellian plasma in an isotropic situation. However these conditions are usually violated in plasma discharges where dust particles are trapped in the sheath of the plasma above the lower electrode, where the ion motion is directed toward the electrodes. Moreover, the electron distribution function for these discharges is not a pure Maxwellian, and are often better characterized by a bi-Maxwellian distribution. In the next section the case is discussed where the ion distribution is not isotropic and there is an ion flow in one direction. This situation is very similar to that which occurs in plasma discharges.

2.3.2 OML Theory in a Flowing Plasma

In the previous section we explained OML theory for a spherical dust grain in a homogeneous and isotropic plasma. In this section we will consider a more general case in which ions have a streaming speed in one direction toward the dust grain. This situation occurs in the plasma sheath where ions accelerate through the sheath toward the boundary. In this case, the ion velocity distribution function is no longer given by Eq. 2.20, and is modified as

$$f_i(v_i) = (\frac{m_i}{2\pi k_B T_i})^{3/2}\exp(-\frac{m_i(\mathbf{v_i} - \mathbf{v_d})^2}{2k_B T_i} - \frac{q_i\phi_s}{k_B T_i}) \tag{2.24}$$

where v_d is the ion flow velocity. Following the same method as used in the previous section, the ion current to the surface of the dust can be calculated. For negatively charged dust particles, the ion current is calculated to be

$$I_i = 4\pi r_d^2 q_i n_i (\frac{k_B T_i}{2\pi m_i})^{1/2}[F_1(\zeta_0) - F_2(\zeta_0)\frac{q_i \phi_s}{k_B T_i}] \tag{2.25}$$

where

$$F_i(\zeta_0 = v_0/(\sqrt{2T_i/m_i})) = (\sqrt{\pi}/4\zeta_0)(1 \ + \ 2\zeta_0^2)erf(\zeta_0) + 1/2 \ \exp(-\zeta_0^2) \tag{2.26}$$

and

$$F_2(\zeta_0) = (\sqrt{\pi}/4\zeta_0)erf(\zeta_0) \tag{2.27}$$

in which $erf(\zeta_0)$ is the error function and is given by $(2/\sqrt{\pi})\int_0^{\zeta_0} \exp(-t^2)dt$ [1].

If the ion streaming velocity is large compared to the ion thermal velocity ($\sqrt{2T_i/m_i}$), then $\zeta_0 \gg 1$ and the ion current can be approximated as

$$I_i = \pi r_d^2 q_i n_i v_d (1 - \frac{2q_i \phi_s}{m v_d}), \tag{2.28}$$

while for the case $\zeta_0 \ll 1$, when ion streaming velocity is much smaller than the ion thermal velocity, Eq. 2.27 reduces to Eq. 2.23.

The effect of ion flow on the charging of the dust particle depends on the ion flow velocity. As shown in Fig. 2.3, as the flow velocity increases, the charge of a single spherical dust particle increases and then decreases [31, 32, 33]. This can be explained as follows: the increase in the charge for lower velocities is due to the geometry; the ion's collection cross section reduces to the dust particle size leading to a more negative charge on the dust. For larger velocities, the ion flux increases, while the electron flux remains almost the same [31].

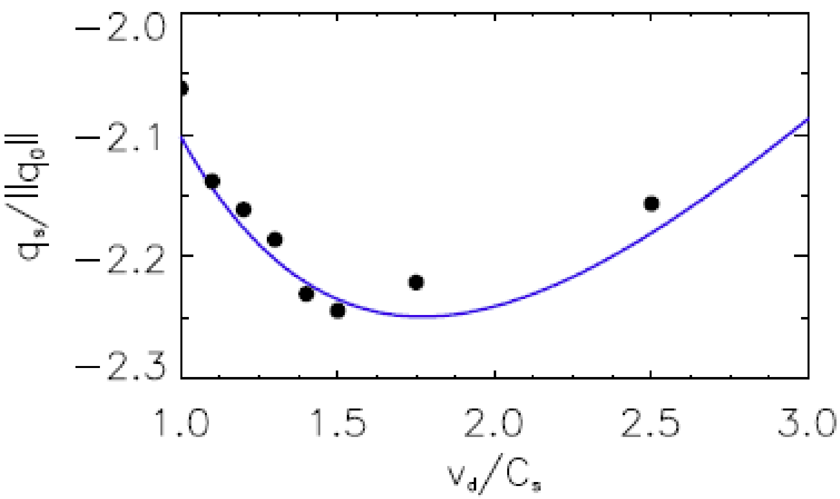

Figure 2.3: Simulation results for the charge on dust in the presence of ion flow as a function of the ion velocity v_d. The dust charge, q_s, is normalized by the absolute value of the charge of the dust in the uniform plasma condition while the ion flow velocity is normalized by the sound speed, $C_s = \sqrt{kT_e/m_i}$. The dots present the simulation results and the solid line shows the results calculated with the OML and capacitance models. Figure adapted from [31].

2.3.3 Secondary Electron Emission

Secondary electron emission is a result of the impact of energetic plasma particles with a dust grain. During the collision, the plasma particle's energy is transferred to other electrons, releasing them from the surface of the dust (Fig. 2.4).

The current of secondary electrons I_s is related to that of primary electrons current, I_e, through the relation $I_s = \delta I_e$ in which δ is the secondary emission coefficient determining the number of emitted electrons per incident electron which depends both on the energy of primary electrons, E, and the dust particle material. However, the dependence on the primary electron's energy, $\delta(E)$, turns out to be practically universal for different materials and is given by [35]

$$\delta(E) = 7.4\delta_m \frac{E}{E_m} \exp(-2\sqrt{\frac{E}{E_m}}) \tag{2.29}$$

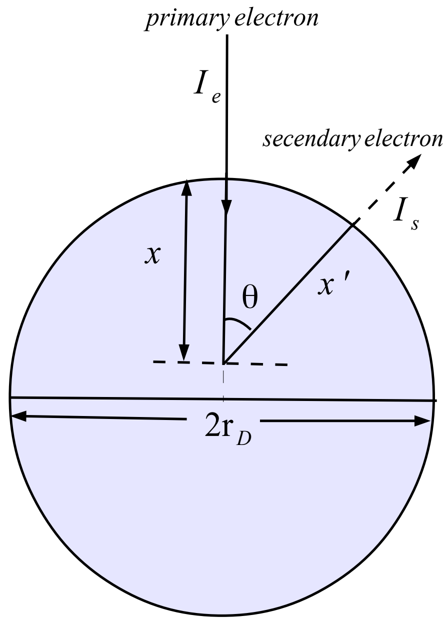

Figure 2.4: A model geometry for secondary electron emission from a spherical dust grain. The primary electron impacts the surface of the dust and penetrates into the dust grain a distance x.The energy lost by the primary electron excites a secondary electron which travels a distance x' to reach the surface of the dust at angle θ and escape from it.

where δ_m is the peak yield at energy E_m. Thus if δ is normalized by the maximum number of electrons, δ_m, then E is normalized by the value of the energy, E_m, at which δ_m is reached. Both of these parameters are material dependent constants. For instance graphite has $\delta_m = 1$ and $E_m = 250\ eV$ [34].

The number of secondary electrons which reach the surface of the material from inside and escape from it decreases exponentially with the distance from the surface to the bulk of the material. It has been shown that secondary emission from small particles is enhanced significantly above the value for bulk materials as particles can escape from both the front and back of the grain [35].

Assuming a Maxwellian distribution function for electrons and ions and including secondary currents into the charging balance, the particle potential can become positive. For Maxwellian electrons, the reversal in polarity generally occurs at an electron temperature of 1 to 10 eV [34].

2.3.4 Photoelectric Emission

Photoelectric emission is a charging process which occurs when photoelectrons absorb UV radiation and escape from the surface of the dust. This also causes the dust particle to become positively charged. Emission of electrons depends on the material properties of the dust particle as well as a particle's surface potential and surface area. It also depends on the energy of photons ($h\nu$) such that the condition for secondary electrons to be emitted is given by $h\nu > W_f + q_d e/r_d$ where W_f is the photoelectric work function of the material of the dust grain, e is the magnitude of electron charge, h is the Planck's constant and ν is the photon frequency [36].

When the dust grain surface potential is positive, $\phi_s > 0$, the most energetic photoelectrons overcome the dust potential and escape from the surface of the dust, but lower energy electrons return to the dust grain. As a result, the net current is determined by the balance between escaped and returned photoelectrons and reads [38]

$$I_p = \pi r_d^2 e \Gamma_p \zeta_{ab} Y_p \exp(-\frac{e\phi_s}{k_B T_p}) \tag{2.30}$$

where Γ_p is the flux of photons, ζ_{ab} is the photon's efficiency of photon absorption, Y_p is the yield of photoelectrons and T_p is the average temperature of photons. To derive this relation, it is assumed that photo-emitted electrons follow a Maxwellian distribution with the temperature T_p where photon temperature is defined as the temperature of the black body from which the photons appear to be emitted.

For a negatively charged dust gain with $\phi_s < 0$, all the photoelectrons escape from the surface into the plasma and none of them return to the surface. This results in a constant current

$$I_p = \pi r_d^2 e \Gamma_p \zeta_{ab} Y_p. \tag{2.31}$$

2.4 Charge Equilibrium

As mentioned above, when a dust particle is placed in a plasma, it collects plasma species flowing onto its surface by acting as a probe, and therefore becomes charged. The change in the dust particle charge, q_d, can then be derived from

$$\frac{dq_d}{dt} = \Sigma_j I_j \tag{2.32}$$

where I_j is the jth plasma species current to the surface of the dust. At equilibrium the total current flowing onto the surface of the dust becomes zero, meaning

$$\frac{dq_d}{dt} = 0. \tag{2.33}$$

This means that the dust surface acquires an equilibrium potential, $\phi_s = q_d/C$ in which C is the capacitance of the dust particle in the plasma. For a spherical dust grain with radius r_d immersed in a plasma, the capacitance C is

$$C = 4\pi\epsilon_0 r_d \exp(-\frac{r_d}{\lambda_D}). \tag{2.34}$$

Substituting Eqs. 2.22 and 2.23 into Eq. 2.32, for a hydrogen plasma where $T = T_e \approx T_i$ the surface potential is found to be [22]

$$\phi_s = -2.51\frac{k_B T}{e}. \tag{2.35}$$

2.5 Numerical Determination of Dust Grain Charge: OML_LOS

As discussed before, the current to a dust grain can be found from Orbital Motion Limited theory (OML). For a single spherical dust grain the current to the surface of the dust can be calculated analytically using Eqs. 2.22 and 2.23. However, for a dust aggregate, because of its complex structure, the current must be obtained through numerical simulation. One of these models is the charging code OML_LOS. The equation for the ion/electron flux can be rewritten as

$$J_{i/e} = n_{i/e,\infty} q_{i/e} \int_{v_{min,i/e}}^{\infty} f_{i/e} v_{i/e}^3 dv_{i/e} \int \cos(\theta) d\Omega, \tag{2.36}$$

with i/e referring to ions and electrons respectively. By specifying the ion/electron distribution function, the integral over velocity can be carried out. The calculation of charge current then reduces to determining $d\Omega = sin(\theta)d\theta d\phi$ for a given point on the aggregate.

The spatial integral over the solid angle, $d\Omega$, is called the LOS (Line Of Sight) factor [37]. LOS factor is used to determine which orbits to include in the limits of the integral. As OML theory assumes that the plasma species orbits connect back to infinity, the LOS factor is used to determine directions in which orbits are not blocked by other parts of the aggregate along straight-line paths. This approximation is less accurate for highly charged dust grains since the orbits of ions/electrons are affected by the electric potential of the dust. Open lines are illustrated in Fig. 2.5 for three different points on a monomer in a dust aggregate. After calculating the open LOS for each point on a constituent monomer, the integral over the angles is carried out. The total charge of the aggregate is then derived by summing the charge on each constituent monomer. This also gives the possibility of calculating the electric dipole moment, $\vec{p}$, of the dust aggregate composed of N monomers using the following relation

$$\vec{p} = \Sigma_{i=1}^{N} \vec{r}_i q_i \tag{2.37}$$

where q_i is the total charge on the ith monomer with its center at $\vec{r}_i$ in the center of mass coordinate system.

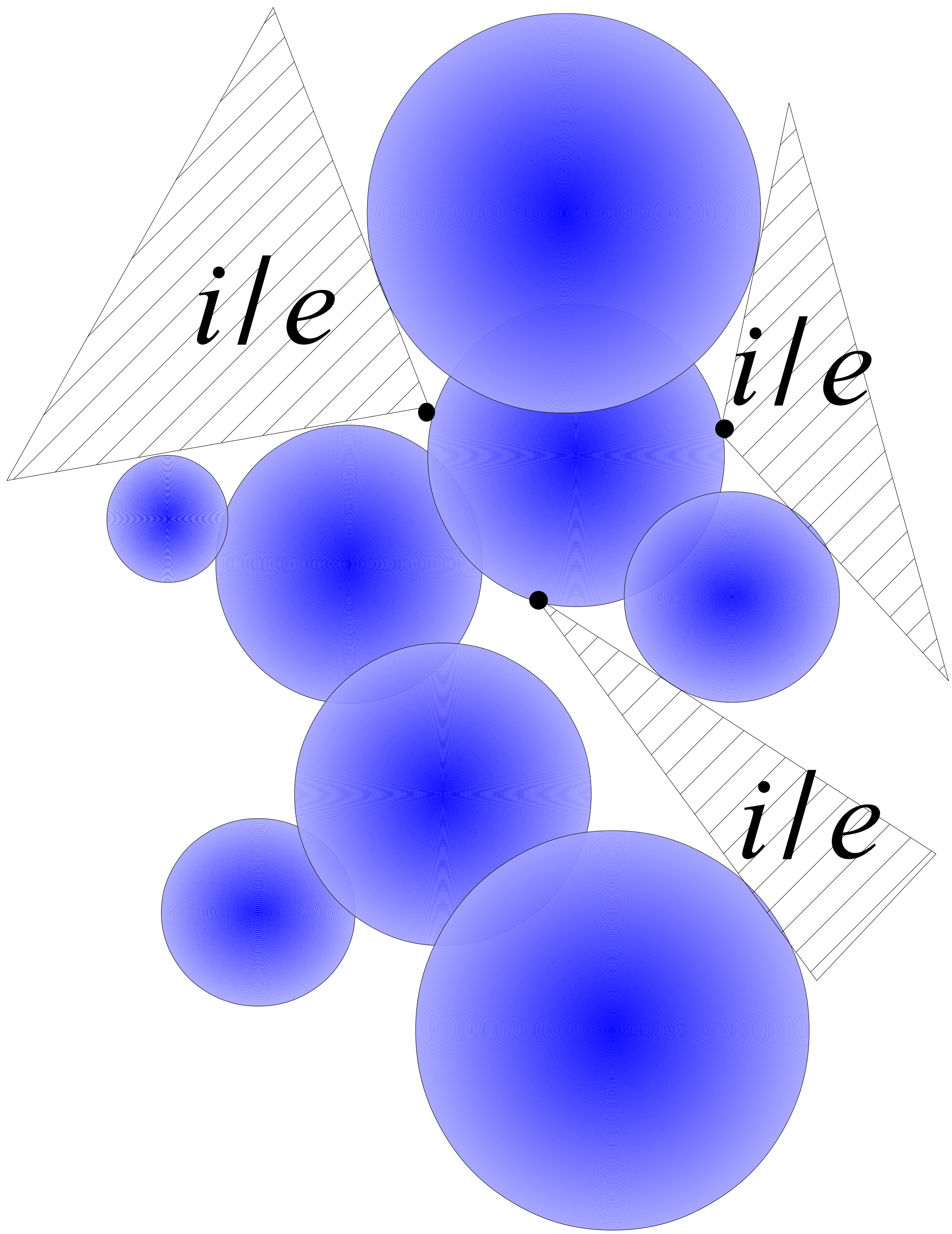

Figure 2.5: In a 2D cross section of a dust aggregate, the LOS factor is determined by finding the unblocked trajectories of ions/electrons incident from infinity to given points on the monomer. The shaded regions indicate the contributions to the LOS factor for three points on a monomer's surface.

CHAPTER THREE

Dynamics of Dust

Dust particles are often trapped in the plasma sheath where the strong electric field arising from the charged lower electrode is balanced by the gravitational force. Additional confinement in the horizontal direction is provided either by a shallow depression in the lower electrode or by a glass box placed on top of the lower electrode. By changing the power delivered to or the gas pressure within the cell, the charge accumulated on the bounding surface and the Debye shielding length can be changed, modifying the dust confinement

Fig. 3.1 shows a schematic of different barriers with various geometries resulting in different dust structures. In this work, all the experiments have been performed in the lower sheath of a capacitive RF discharge using a glass box to provide the horizontal confinement. The different dust structures formed, and their interaction with the plasma and confining electric fields, are discussed in detail in the following chapters.

3.1 Forces on Dust

Charged dust particles in a plasma experience different forces which can be divided into two groups: those which depend on the electrostatic properties of the dust such as electrostatic force and ion drag, and those which are independent of the particle charge, such as gravity, the neutral drag force, thermophoresis, and the force imparted by a laser. By analyzing these forces under given plasma conditions, it is possible to measure the electrostatic properties of the dust including electric charge and dipole moment as well as plasma parameters such as the electric field in the sheath.

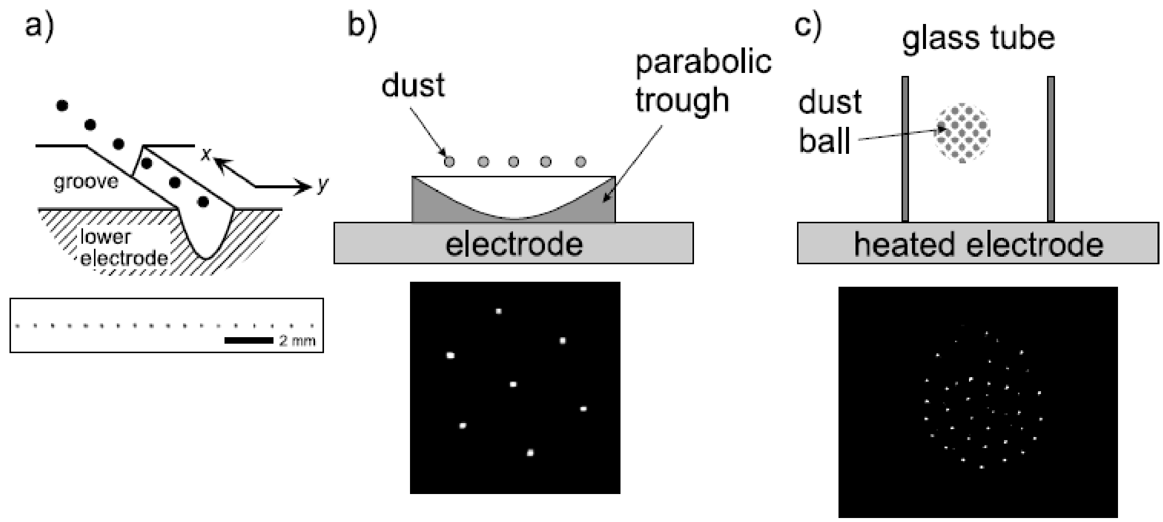

Figure 3.1: One, two and three dimensional particle structures formed under different confinement geometries. a) One dimensional cluster composed of 18 dust particles formed horizontally as a result of a groove in the lower electrode. b) A two dimensional cluster composed of 7 particles formed in the horizontal direction resulting from a hyperbolic cutout placed on top of the lower electrode. c) Three dimensional dust ball composed of many ($\sim$ 190) dust particles confined by a glass tube placed on top of the lower electrode. Figure adapted from [35].

3.1.1 Electric Field Force

The electrostatic force is due to the interaction between the charge of the dust and any external electric field, $\vec{E}$, in the plasma. Generally this is one of the governing forces which controls the motion of the dust and is given as

$$\vec{F}_E = q_d \vec{E}. \tag{3.1}$$

It should be noted that $F_E \propto r_D$ since $q_D \propto r_D$. In the bulk of the plasma, the electric field is negligible as a result of quasi-neutrality. Thus, for large particles where gravity is considerable, levitation of the dust occurs in the sheath of the plasma where the total electric field is quite strong, providing a counter balance against gravity. The electric force is commonly a combination of external electric fields including electric fields due to the other dust particles, as well as the electric field of any solid boundary in the sheath.

3.1.2 Ion Drag Force

The ion drag force arises from the relative motion of ions, in the form of an ion stream, with respect to the dust particle. When an ion streams past a dust particle, it is either scattered or collected by the surface of the dust, transferring a momentum to the dust. The ion drag force consists of two parts, the Coulomb force, $\vec{F}_{Coul}$, arising from scattered ions and a collection force, $\vec{F}_{coll}$, due to ions hitting the surface of the dust [39, 40, 41, 42]. Therefore, the total drag force is

$$\vec{F}_{ion} = \vec{F}_{Coul} + \vec{F}_{coll} \tag{3.2}$$

The Coulomb force arises from interaction of ions with the local electric field in the sheath surrounding the dust grain which deflects ions in the ion stream, and is given by

$$\vec{F}_{Coul} = 4\pi b_{\pi/2}^2 m_i v_s n_i ln(\frac{\lambda_D^2 + b_{\pi/2}^2}{b_c^2 + b_{\pi/2}^2})^{1/2}\vec{v}_{0i}. \tag{3.3}$$

Here $b_c = r_d(1 - 2eq_d/(4\pi\epsilon_0 r_d m_i v_s^2))$ is the maximum impact factor and $b_{\pi/2} = q_d q_i/(4\pi\epsilon_0 m_i v_s^2)$ is the impact factor for 90° scattering. $v_s = (v_{0i}^2 + v_{th,i}^2)^{1/2}$ is the geometric mean of the ion streaming velocity v_{0i} and ion thermal velocity $v_{th,i}$.

Ions colliding with the surface of the dust contribute to ion charging of the dust, but this is not the only effect of their collision. They also transfer momentum to the dust and consequently exert a force which is given by

$$\vec{F}_{Coll} = \pi r_d^2 m_i v_s n_i (1 - \frac{2e\phi_f}{m_i v_s^2})\vec{v}_{0i} \tag{3.4}$$

where ϕ_f is the steady state or time-dependent potential of the dust [43].

As shown in Fig. 3.2, the ion drag force has been measured experimentally by dropping particles through a plasma discharge. Ions flow toward the boundaries of the plasma. At higher powers the flowing ions become more energetic and they collide with the dust particles more often and push them in the same direction that they

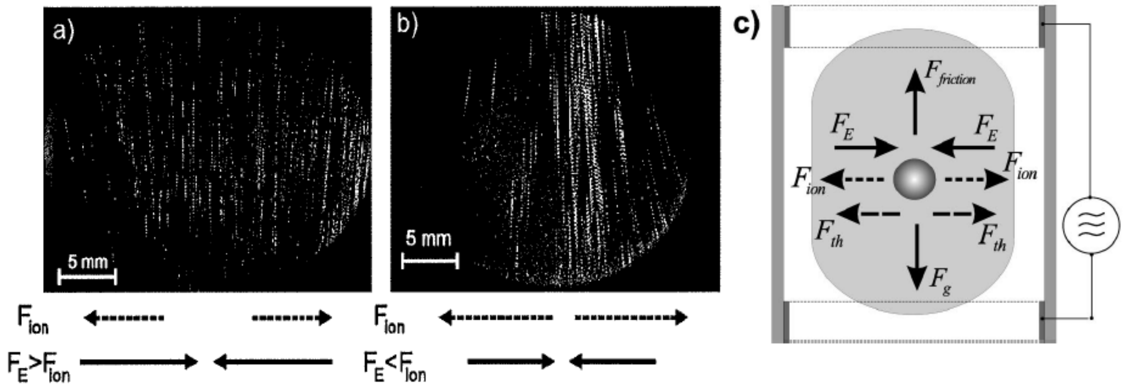

Figure 3.2: Dust particles dropped through a discharge plasma at 2 W (a) and 5 W (b) with a schematic of the forces acting on the dust particle (c). As shown in the figure, at lower powers the confinement electric field force pushes the particles toward the center while at higher powers the trajectories of dust particles are affected by the ion drag force, being pushed away from the center. Figure adapted from [21].

are moving. Thus at higher power the ion drag force is dominant, while at lower operating powers the electric field force exceeds the ion drag force.

3.1.3 Gravity

The gravitational force is

$$\vec{F_G} = m_d\vec{g} = \frac{4}{3}\pi r_d^3 \rho_d \vec{g} \tag{3.5}$$

where $\vec{g}$ is the gravitational acceleration at the surface of the earth and ρ_d is the mass density of the dust. As F_G is proportional to r_d^3, for larger dust particles in the micrometer size range, the gravitational force is one of the dominant forces.

3.1.4 Neutral Drag Force

The neutral drag is the resistive force a dust particle experiences when it moves through a gas. If the size of the dust is much smaller than the mean free path of the gas molecules ($r_d \ll \lambda_{mfp}$) and the velocity of the dust is much smaller than the thermal velocity of the gas ($v \ll v_{th,n}$), then the drag force acting on a dust particle moving with velocity v_D is derived using Epstein's relation [44, 45]

$$\vec{F}_D = -m_d \beta \vec{v}_D \tag{3.6}$$

where β is the damping coefficient and is given by

$$\beta = \delta \frac{8\pi p}{\pi r_d \rho_d v_{th,n}} \tag{3.7}$$

in which the parameter δ measures the probability of a perfect diffuse reflection and depends on the surface properties of the dust particle, and p is the gas pressure.

3.1.5 Thermophoresis

The thermophoretic force occurs when there is a temperature gradient in the neutral gas so that the gas molecules coming from the direction with a greater temperature have a higher thermal velocity compared to those incident from the direction with a lower temperature. As a result, a net momentum is transferred to the dust particle directed toward the region of colder gas. From gas kinetic theory, when the mean free path of the gas molecules λ_{mfp} is much larger than the dust radius, this force is given as [46, 47]

$$\vec{F}_T = -\frac{32 r_d^2 k_n}{15 v_{th,n}} \vec{\nabla} T_n \tag{3.8}$$

where $\vec{\nabla} T_n$ is the temperature gradient in the gas and k_n is the thermal conductivity of the gas. The thermophoretic force is important for submicron sized particles when the plasma discharge heats the gas [22] and can also be utilized as an additional levitation force by heating the lower electrode [48].

3.1.6 Laser Forces

In many dusty plasma experiment a laser is used to manipulate dust particles, either directly through radiation pressure or indirectly through the photophoretic force. Radiation pressure, P_{rad}, is the result of momentum of the incident photons transferred to the dust and is given by [29]

$$P_{rad} = \frac{I}{c} \tag{3.9}$$

where I is the laser intensity and c is the speed of light.

For transparent dust particles, radiation pressure can have a component perpendicular to the direction of the incident laser beam. The laser beam intensity has a maximum at the center of the beam and it becomes weaker outward. If the laser beam is focused on the top portion of a transparent dust particle, more photons are deflected downward from the top portion of the dust compared to the lower part and as a result the radiation pressure force pushes the particle in the direction perpendicular to the beam.

The photophoretic force, which results from heating the surface of the dust, has a similar mechanism as the thermophoretic force discussed above. The incident photons heat the illuminated side of the dust which leads to a temperature gradient across the particle. When neutral gas particles hit the "hot" side of the dust, they are re-emitted with a higher velocity. This leads to a force in the direction of the laser beam, away from the hot side of the dust. The photophoretic force can be written as [29]

$$F_{ph} = \frac{\pi r_d^3 I p}{6(p r_d v_{th,n} + \kappa T)} \tag{3.10}$$

where p is the gas pressure, κ is the thermal conductivity of the dust particle, and T is the gas temperature. It is very difficult to distinguish the dominant force between photophoretic and radiation pressure forces. However, lasers are used widely to manipulate dust particles in the laboratory.

3.2 Torques on the Dust

As a dust grain in a dusty plasma experiences different forces, it might be subject to a torque which causes it to rotate. This phenomenon has been observed for irregular aggregates in many experiments [49, 50, 51, 52, 53]. The total torque acting on a dust particle is given by

$$\frac{d\vec{\mathbb{L}}}{dt} = I\vec{\alpha} = \sum_i \vec{\tau}_i \tag{3.11}$$

where $\vec{\mathbb{L}}$ is the angular momentum, I is the moment of inertia of the dust about the axis of rotation, and $\vec{\tau}_i = \sum_i \vec{r}_i \times \vec{F}_i$ is the torque due to the ith force, F_i, which acts at a point with perpendicular distance r_i from the axis of rotation. The forces applied to the dust can include any of the forces explained briefly in the previous sections. However, in the following we will present the torques due to the electric field force as well as the neutral drag force.

3.2.1 Electric Field Torque

A charged dust grain may have an electric dipole moment, due to a non-uniform charge distribution. Such a charge distribution could be caused by the irregular geometry of the dust grain or due to anisotropic charging. Therefore, in the presence of an external electric field, under specific conditions, the electric field force can apply a torque on the particle causing the particle to rotate. In this case, the torque, $\vec{\tau}_E$, is governed by

$$\vec{\tau}_E = \vec{p} \times \vec{E} \tag{3.12}$$

where $\vec{p}$ is the electric dipole moment of the dust and $\vec{E}$ is the external electric field in the vicinity of the dust. This electric field can be due to the electric filed from the lower electrode or other plasma boundaries or due to the proximity of another charged grain.

3.2.2 Neutral Drag Torque

As a particle moves through a gas, it experiences a neutral drag force. For a dust grain rotating with an angular velocity $\vec{\omega}$, even if the center of rotation is at rest in the lab coordinate system, the parts of the particle are in relative motion with respect to the center of rotation. Consequently, they will experience a drag force, and as a result, a drag torque. The total torque on the dust is given by

$$\vec{\tau}_D = \sum_i \vec{r_i} \times \vec{F}_{Di} \tag{3.13}$$

with $\vec{r_i}$ being the perpendicular distance from the center of each patch to the vertical axis, about which the dust particle is rotating. It is clear that a drag torque tends to decrease the angular velocity.

A dust aggregate is assumed to be a composition of monomers with a symmetric structure. In the experiments studied here, the monomers are spherically symmetric. As a result, in Eq. 3.13, i refers to each monomer as a sub-unit, $\vec{r_i}$ is the vertical distance from center of each monomer to the axes of rotation, and $\vec{F}_{Di}$ is the neutral drag force ith monomer experiences. From Eq. 3.6, $\vec{F}_{Di} = r_i\omega$ in which ω is the angular velocity of rotation.

3.3 Experimental Determination of Dust Grain Charge

So far theoretical concepts of dust particle charging in a plasma have been presented. The experimental study of dust particle charging is very important, especially in cases where many of the plasma parameters are unknown or can not be measured with sufficient accuracy. Experiments also provide a check on different theoretical models.

Dust particle electrostatic characteristics as well as plasma parameters can be determined by studying the behavior of a dust particle in a plasma. The dynamics of a dust particle can be manipulated using different methods such as laser radiation, or adjusting plasma operating conditions to make an ordered structure of dust particles. For instance, the direct determination of the charge on a dust particle has been made experimentally in [54] by analyzing the interaction of two micron-sized spherical dust particles.

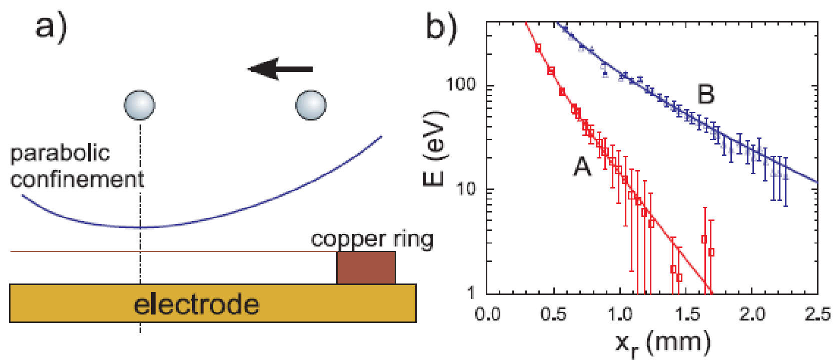

Figure 3.3: Interaction of two spherical dust particles. a) A schematic of the experimental setup. A copper ring is placed on top of the lower electrode in a RF discharge to provide a parabolic confinement. b) The electrostatic interaction energy as a function of relative distance, x_r, between the particles at two different discharge voltages (A and B). Figure adapted from [29].

As shown in Fig. 3.3(a) the experiment is performed in a RF discharge where a copper ring is placed on top of the lower electrode to provide a parabolic radial confinement. One of the two particles was allowed to sit at rest at the center of the confinement, while the other one was pulled away using a positively biased probe and then released. The interaction of the two particles was studied by analyzing the particle trajectories considering force equations for both particles. From electrostatic interaction energy profiles taken at two different discharge voltages, shown in Fig. 3.3(b), the electric charge of the particles were estimated to be 13900 e and 17100 e respectively. In the next two chapters we will present two experiments from which dust particles' electrostatic characteristics, as well as the plasma surrounding them, are determined.

CHAPTER FOUR

Electric Charge and Dipole Moment of Dust Aggregates

This chapter published as: Measurement of net electric charge and dipole moment of dust aggregates in a complex plasma, R. Yousefi, A. B. Davis, J. C. Reyes, L. S. Matthews, and T. W. Hyde, Phys. Rev. E 90, 033101 (2014).

Dust plays a key role in the evolution of molecular clouds and the early stage of star and planet formation. The processes governing the evolution of the system are tied to the properties of the dust grains, such as the size distribution and porosity (fluffiness) of the aggregates [55, 56].

As explained in Chapter Two, in a dusty plasma the dust is charged, either by being immersed in a radiative or plasma environment or through triboelectric charging. While the microphysics of the coagulation process is fundamental to all of these areas, it is not yet well understood. One of the reasons for this is due to the fact that a knowledge of the basic properties of the dust particles is required to better understand and explain these phenomena. The particle electrostatic charge and dipole moment are two of the most important parameters which help define the dusty plasma since they determine both the particle interactions with themselves as well as with the plasma particles and existing electromagnetic fields.

In this chapter, experimental data is provided in which dust aggregates are formed from gold coated mono-disperse spherical melamine-formaldehyde monomers in a radio-frequency (RF) argon discharge plasma. The behavior of observed dust aggregates is analyzed both by studying the particle trajectories and by employing computer models examining 3D structures of aggregates and their interactions and rotations as induced by torques arising from their dipole moments. These allow the basic characteristics of the dust aggregates, such as the electrostatic charge and dipole moment, as well as the external electric field, to be determined. It is shown that the experimental results support the predicted values from computer models for aggregates in these environments.

4.1 Previous Analysis

Grains in a plasma environment often attain charges sufficiently large that they are equally affected by local electrical and gravitational fields [57, 58]. One method for calculating the charge of isolated dust grains in a Maxwellian plasma is orbital-motion limited (OML) theory, which has been has been studied for isolated spherical dust grains as described in Chapter Two. Measurement of the charge on dust grains in laboratory experiments has also been performed for both isolated [59] and non-isolated dust grains [60]. For most conditions, experimental results agree fairly well with theoretical predictions.

Dust grains in astrophysical and laboratory plasmas are not necessarily spherically symmetric; the grains are typically elongated [61, 62] or aggregates consisting of many small subunits [63]. It has been shown that aggregates in both laboratory and astrophysical environments tend to acquire more charge compared to spherical grains of the same mass due to their porous structure [64, 65, 66, 67]. A fluffy aggregate, consisting of many spherical monomers, has charge distributed over its irregular surface which leads to a nonzero dipole moment.

It is evident that any proper explanation of dynamics of dust particles requires a fundamental understanding of the electrostatic charge and dipole moment of dust aggregates. The electrostatic charge and dipole moment of individual particles in a cloud of spherical dielectric particles, dispersed in air passing through a non-uniform electric field, has been experimentally measured in [68] by studying the particles' trajectories. In numerical studies, the electric charge and dipole moment of aggregates in a plasma environment have been calculated using modified OML theory [69] and the interaction between two charged grains modeled by calculating the torques and accelerations due to the charged aggregates or external electric fields [67, 70]. However a direct study of both electrostatic charge and dipole of dust particles in laboratory plasmas has not yet been made.

In the following sections, we first review a numerical model to investigate electrostatic properties of dust aggregates, then present a model for the complex plasma environments, where dust aggregates formed in a laboratory plasma and their basic properties are investigated. These results are then compared with an the numerical model.

4.2 Numerical Models

The charging of a single spherical dust grain immersed in a plasma due to the collection of plasma particles was described by OML theory in Chapter Two where Eq. 2.21 gives the ion/electron current to the surface of a spherical dust grain. This model is applied to a dust aggregate by considering the LOS factor to patches on the aggregates and described as OML_LOS in Section 3.3. The total charge of the aggregate is derived by adding the charge on each constituent monomer. This also gives the possibility of calculating the electric dipole moment, $\vec{p}$, of the dust aggregate composed of N monomers using

$$\vec{p} = \sum_{1}^{N} q_i \vec{r_i} \tag{4.1}$$

where q_i is the total electric charge on the ith monomer with its center at $\vec{r_i}$ in the center of mass coordinate system of the dust aggregate.

The interaction between dust aggregates is modeled using $Aggregate - Builder$ code which which incorporates the charge and dipole moments calculated using OML_LOS [69]. The total electric field of each aggregate, $\vec{E}$, is calculated using the monopole and dipole contributions. The electric field will induce an acceleration of the other dust particle as well as a torque, resulting in rotational motion of the aggregate. In addition to the electrostatic force, the gravitational force and gas drag force also contribute in governing the motion of the dust. In each time-step the total force and torque on each aggregate is calculated and the position, velocity, and acceleration of each aggregate is updated.

4.3 Experiment

The complex plasma experiments are performed in a modified GEC (Gaseous Electronics Conference) RF reference cell, with the setup shown in Fig. 1.7. The vacuum chamber lower cylindrical electrode is driven at a frequency of 13.56 MHz and the hollow cylindrical upper electrode is grounded.

Single gold-coated melamine formaldehyde (mf) spheres with mass of $6.10 \pm 0.09 \times 10^{-13}$kg, are introduced into the argon plasma from a shaker located above the upper electrode. The dust particles are confined inside a one inch open-ended glass box placed on the lower electrode. The plasma is typically maintained at a RF peak-to-peak voltage of 80 V and a pressure of 500 mTorr, allowing the particles to form a stable cloud within the box.

Using the same method as reported in [71] for creating the aggregates, the particles are accelerated by triggering self-excited dust density waves by rapidly decreasing the pressure to 50 mTorr. After several minutes the pressure is returned to the initial level, and aggregates consisting of up to $\approx$20 monomers are observed. Aggregates are back-lit using a 500 W flood lamp and imaged using a CMOS monochromatic high speed camera (1024 FASTCAM Photron) at 3000 fps.

To ensure that aggregates form within the focal plane of the camera and lens assembly, the glass box is placed off-center on the lower electrode, closer to the window where the camera is mounted. The recorded field of view spans an area of 717 μm $\times$ 829 μm with a resolution of 1.4 μm/pixel. The aggregates and their interactions are sampled randomly as the particles move through the focal plane of the camera, which is less than 500 microns deep and very small compared to the size of the box.

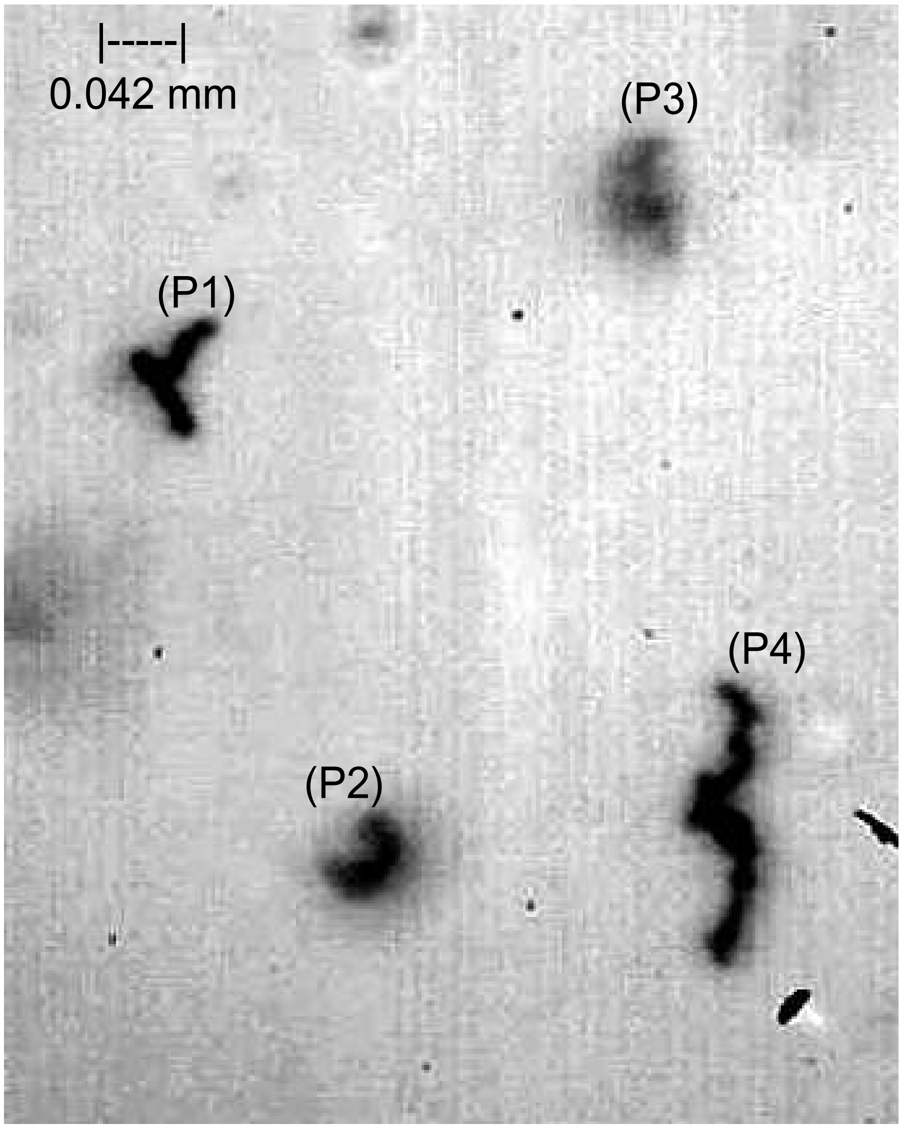

Figure 4.1: A representative single frame of rotating aggregates showing four particles. Rotation of P1 -P3 about the vertical axis was observed, while P4 was moving from right to left without any rotation, probably due to its small horizontal electric dipole moment.

In the experiment, observed aggregates tend to be linear and elongated. Individual aggregates are often observed to rotate about the vertical z-axis, with a rotation period of approximately a few hundredths of a second. A representative sample of the aggregates observed is shown in Fig. 4.1. Aggregate rotation allows three-dimensional models to be reconstructed, as illustrated in Fig. 4.2. Spherical monomers are used to match the projected 2D orientation of an aggregate over several frames as it moves and rotates, with the final positions of the monomers adjusted so that each monomer is connected at at least one point. Interacting aggregate pairs exhibit rotation induced by their charge-dipole interactions as shown in Fig. 4.3.

4.4 Analysis

In order to better understand the dynamics of dust particles, a schematic of the experimental setup is shown in Fig. 4.4, where the dominant forces acting on a dust particle are presented.

In the experiment, the rate of change of the center of mass velocity $\vec{v}$ for particles with mass m and charge q, was calculated using the equation of motion including the dominant forces acting on the particle. These forces include gravity, $\vec{F}_G$, gas drag, $\vec{F}_D$, and the electrostatic force, $\vec{F}_E$,

$$m\frac{d\vec{v}}{dt} = \vec{F}_G + \vec{F}_D + \vec{F}_E. \tag{4.2}$$

For weakly ionized plasmas, we consider only neutral gas drag since it dominates the ion drag [72]. The neutral drag force is given by the Eq. 3.6 in which β was determined experimentally for a single mf sphere. Using the same method as described in [73], a laser was used to perturb a dust grain, which oscillated about its equilibrium position. Fits to the damped oscillatory motion were used to find $\beta = 9.8 \pm 0.9\ s^{-1}$. Since β is proportional to the cross-sectional area of spherical particles, the drag

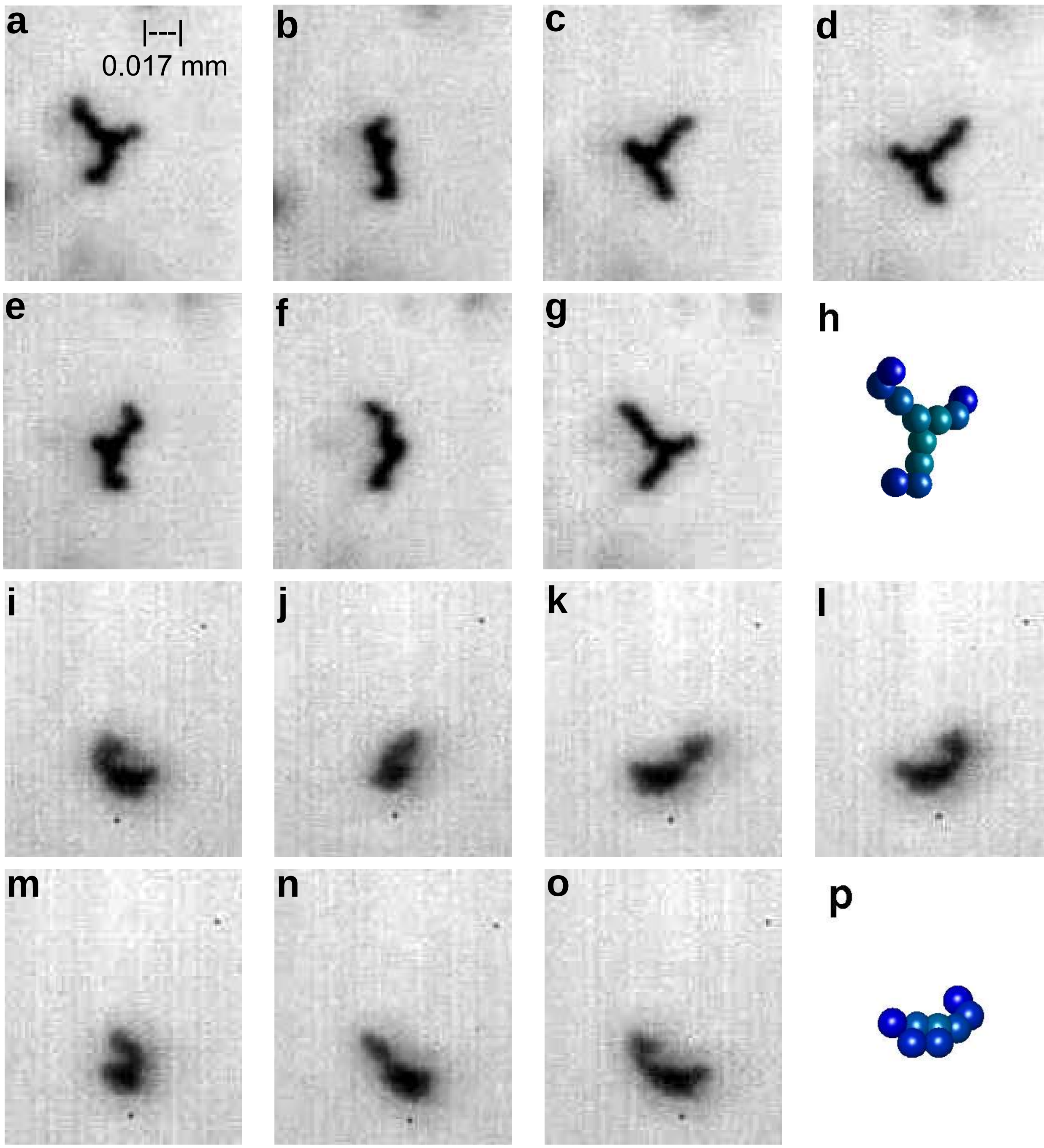

Figure 4.2: $(a-g)$ Sequence of images showing the complete rotation of cluster $P1$ from Fig. 4.1 consisting of eleven 8.93 μm gold-coated mf particles, ($\Delta t = .0167s$), and (h) its reconstructed 3D model. $(i{-}o)$ $P2$ from Fig. 4.1 consisting of eight particles, ($\Delta t = .0117s$), and (p) its reconstructed 3D model. Spatial scaling is the same for all the sub images.

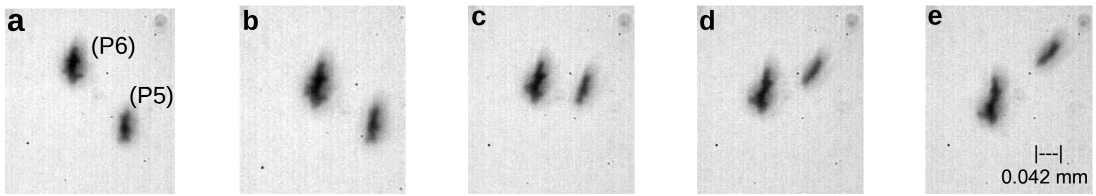

Figure 4.3: A sequence of images showing a sample interaction between two charged dust particles ($P5$) and ($P6$). ($P5$) begins in the bottom right and ($P6$) begins in the top left (Δt=0.001s).

coefficient for larger aggregates is found by scaling β by the projected (2D) cross-sectional area.

The electrostatic force arises from the interaction of dust particle with charge q with the electric field from other dust grains, $\vec{E}_{int}$, the vertical electric field in the sheath above the lower electrode, $\vec{E}_z$, and a confining electric field in the horizontal direction arising from walls of the box, $\vec{E}_r$,

$$\vec{F}_E = q(\vec{E}_{int} + \vec{E}_z + \vec{E}_r) \tag{4.3}$$

Assuming a screened Coulomb potential around each dust particle, the electric field produced by a charged particle is

$$\vec{E}_{int} = \frac{q}{4\pi\epsilon_0}\{\frac{\vec{r}}{r^2} + \frac{\vec{r}}{r\lambda}\}\frac{e^{-\frac{r}{\lambda}}}{r} \tag{4.4}$$

where r is the radial distance from the center of the particle and λ is the screening length, which is estimated to be equal to the electron Debye length, $\lambda_D = (kT_e\epsilon_0/n_e e^2)^{1/2}$, due to high mobility of electrons in the plasma sheath where dust particles are levitating [74, 75, 76]. $\vec{E}_r$, the confining electric field due to the Yukawa potential inside the box arising from the negative charges on the walls of the box [77] and $\vec{E}_z$, the vertical electric field, are taken to be unknown in all the calculations.

The rotation of a particle is driven by the total torque acting on the dust particle as given by Eq. 3.13 in which

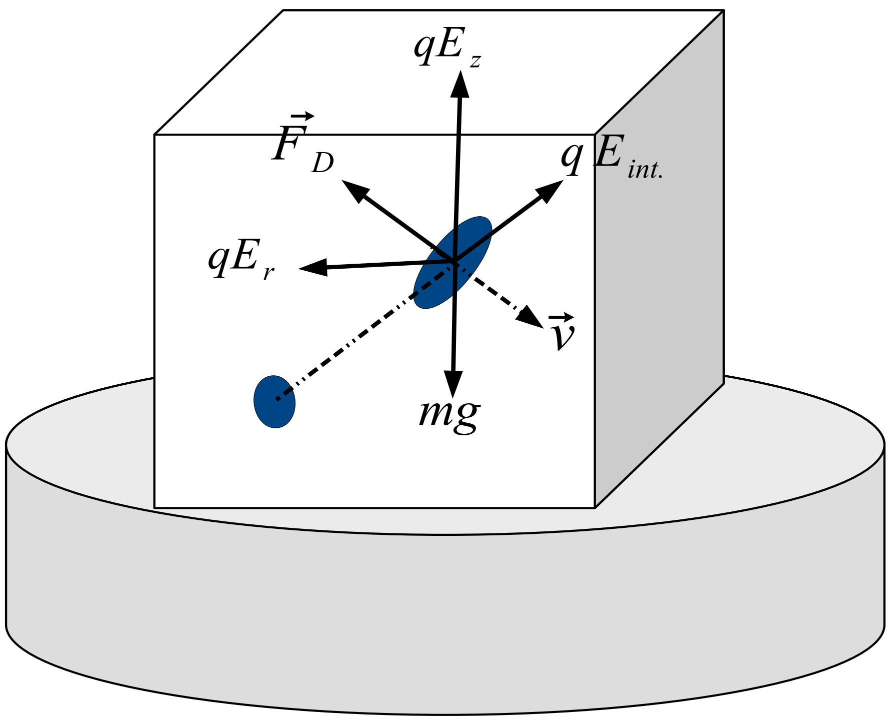

Figure 4.4: A schematic of the lower electrode and a glass box placed on top of it. Dust aggregates are symbolized by the blue ovals. The dominant forces exerted on a particle are indicated.

$$\sum_i \vec{\tau_i} = \vec{\tau}_E + \vec{\tau}_D \tag{4.5}$$

where $\vec{\tau}_E = \vec{p} \times \vec{E}$ is the torque due to the electric field including $\vec{E}_{int}$, $\vec{E}_z$ and $\vec{E}_r$, and $\vec{\tau}_D = \sum_i \vec{r_i} \times \vec{F}_D$ is the torque due to the drag force, with $\vec{r_i}$ being the perpendicular distance from the center of each monomer to the vertical axis passing through the center of mass, about which the aggregate is rotating.

4.5 Results

For rotating aggregates, a sequence of 500 image frames was analyzed using ImageJ [78]. A number of aggregates, almost fixed in place, spinning about the vertical z-axis with a nearly constant angular velocity were observed (Fig. 4.1). Two of the particles, $P1$ and $P2$, which are in focus were examined using the 3D models shown in Fig. 4.2(h) and 4.2(p). The total charge on these rotating aggregates was estimated numerically using the OML_LOS code to be $q_1 = -0.82 \times 10^{-14}$ C and $q_2 = -0.59 \times 10^{-14}$ C, respectively. Since these aggregates show little vertical or horizontal translational motion, the gravitational force acting on the particles is assumed to be balanced by the electrostatic force due to the vertical electric field. Using this fact, the magnitude of the vertical electric field corresponding to the position of each aggregate is estimated to be $E_{z1} = 0.80 \times 10^4$ V/m and $E_{z2} = 0.81 \times 10^4$ V/m. The resulting electric field gradient is consistent with the results reported in [79]. The Debye length of the plasma is estimated to be about 0.1 mm using the values of T_e, T_i, n_e and n_i given in section III. The minimum distance between the rotating aggregates in the 2D images is measured to be $\sim$ 0.3 mm, which is several times larger than the estimated Debye length. Therefore it is reasonable to assume that $\vec{E}_{int}$ is negligible between the particles.

Non-interacting aggregates are only observed to rotate about a vertical axis passing through the center of mass. The gravitational force, acting at the center of mass, and vertical electrostatic force, acting at the "center of charge" exert opposing forces

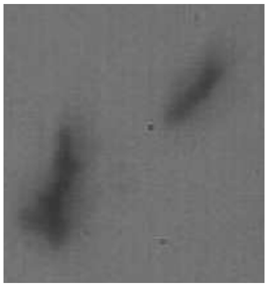

(a) Raw image

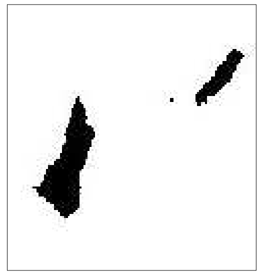

(b) Binary image

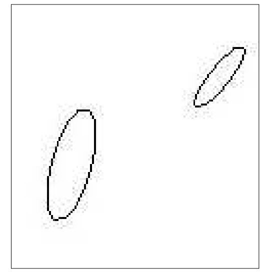

(c) Analyzed image

Figure 4.5: Illustration of image processing. (a) A raw image loaded into ImageJ. (b) Binary image after setting a pixel value threshold in the program for the image shown in (a). (c) Image analysis by fitting ellipses snugly around the detected aggregates in (b) through "Analyze Particle" function.

and an aligning torque with any rotation about a horizontal axis damped by gas drag. The force exerted by the horizontal electric field causes a rotation about the vertical axis, and damping from gas drag causes an aggregate to spin at a constant rate. The rotational angular velocity is measured by determining the number of frames ($\pm$ frame) for a spinning aggregate to return to its initial orientation averaged over four complete rotations. Previous experiments with the same experimental conditions estimated the magnitude of the horizontal electric field to be $\mid \vec{E}_r \mid= 100$ V/m [77]. Using this value in Eq. (4.5) and calculating the drag force as described for the 3D model allows the magnitude of the electric dipole moment in the horizontal plane to be calculated, resulting in values of $\mid \vec{p}_{1r} \mid= 3.15 \times 10^{-19}$ Cm and $\mid \vec{p}_{2r} \mid= 0.31 \times 10^{-19}$ Cm with 25% uncertainty due to a combined uncertainty in E_r, drag force, and angular velocity. These values are in very good agreement with the values predicted by OML_LOS, $\mid \vec{p}_{1r} \mid= 3.1 \times 10^{-19}$ Cm and $\mid \vec{p}_{2r} \mid= 0.29 \times 10^{-19}$ Cm. It is interesting to note that the value of the horizontal electric dipole moment for $P4$, which is observed to have no rotation during the measured time frame, is predicted to be $\mid \vec{p}_{1r} \mid= 0.09 \times 10^{-19}$ Cm by OML_LOS. The small value of the horizontal electric dipole moment could be one reason for the lack of rotation.

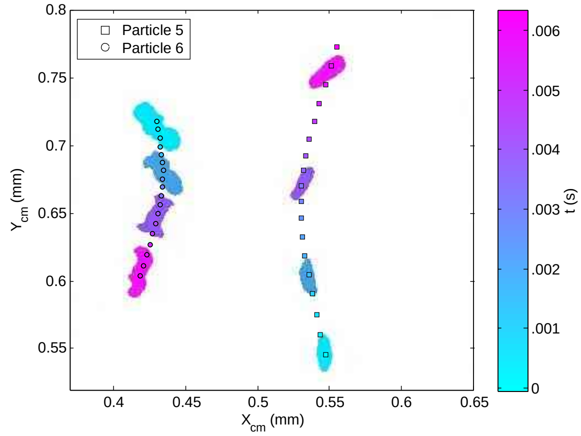

Figure 4.6: Time evolution of the X- and Y-components of center of mass position for two interacting particles, P5 and P6, superposed on four frames from Fig. 3, with color indicating the time.

For the interacting aggregate pairs, a 30-frame sequence of images, showing a short interaction between two charged dust particles, $P5$ and $P6$, was analyzed using ImageJ. As shown in Fig. 4.3, $P5$ enters the frame from the lower right and $P6$ enters the frame from the upper left. As they approach one another, their paths are deflected. $P5$'s rotation about an axis perpendicular to the image plane is considerable. A pixel value threshold was set in the program to convert the gray-scale image into a binary image (4.5(b)). The "Analyze Particles" function in ImageJ was then used to fit ellipses snugly around the particles detected as shown in Fig. 4.5(c) to determine the center of mass coordinates and orientations, and the angle between the ellipse's major axis to the horizontal axis for all the particles in each frame. Fig. 4.6 shows the center of mass positions X_{cm} and Y_{cm} ($\pm 5.6 \mu m$) for both particles as they change over time overlaid on four frames from the movie, with their orientation as a function of time shown in Fig. 4.7. A polynomial function was fit to the X- and Y-position as a function of time for each particle, with velocity and acceleration of the particles derived by differentiating these equations [80].

The two vector-component equations from Eq. (5.4) for the two particles gives the following set of equations

$$
\begin{aligned}
\ddot{x}_5 &= -\beta\dot{x}_5 \\
&\quad + \frac{q_5 q_6}{4\pi\epsilon_0 m_5}\{\frac{1}{r^2}+\frac{1}{r\lambda}\}\frac{e^{-\frac{r}{\lambda}}}{r}x_{56}+\frac{q_5 E_r}{m_5}, \\
\ddot{y}_5 &= -\beta\dot{y}_5 \\
&\quad + \frac{q_5 q_6}{4\pi\epsilon_0 m_5}\{\frac{1}{r^2}+\frac{1}{r\lambda}\}\frac{e^{-\frac{r}{\lambda}}}{r}y_{56}+\frac{q_5 E_z}{m_5}-g, \\
\ddot{x}_6 &= -\beta\dot{x}_6 \\
&\quad + \frac{q_5 q_6}{4\pi\epsilon_0 m_6}\{\frac{1}{r^2}+\frac{1}{r\lambda}\}\frac{e^{-\frac{r}{\lambda}}}{r}x_{65}+\frac{q_6 E_r}{m_6}, \\
\ddot{y}_6 &= -\beta\dot{y}_6 \\
&\quad + \frac{q_5 q_6}{4\pi\epsilon_0 m_6}\{\frac{1}{r^2}+\frac{1}{r\lambda}\}\frac{e^{-\frac{r}{\lambda}}}{r}y_{65}+\frac{q_5 E_z}{m_6}-g
\end{aligned}
\tag{4.7}
$$

where x_i and y_i are x and y componet of position of the ith particle, $x_{ij} = x_i - x_j$ and $y_{ij} = y_i - y_j$. The particle's positions, velocities, and accelerations were calculated at the point of closest approach using eight frames of the interaction centered around this time. Substituting these values, along with E_r, into Eq. 6 results in three independent equations

$$
\begin{aligned}
16.3 \times 10^{-29} q_5 q_6 + 20.5 \times 10^{-18} q_5 E_z = -10.3, \\
7.3 \times 10^{-29} q_5 q_6 - 10.2 \times 10^{-18} q_6 E_z = 9.6, \\
q_5 q_6 = 0.4 \times 10^{-28}
\end{aligned}
\tag{4.8}
$$

with three unknown variables: q_5, q_6 and $\vec{E}_z$, where q_5 is the net charge on $P5$ and q_6 is the net charge on $P6$. Solving these equations yields $q_5 = -0.48 \times 10^{-14}\ C$ ($\pm 20\%$), $q_6 = -0.83 \times 10^{-14}\ C$ ($\pm 17\%$) and $\mid \vec{E}_z \mid = 1.11 \times 10^4\ V/m$ ($\pm 25\%$) in the downward direction.

The electric dipole moments of the dust grains are then calculated from the particles' changing orientations during the interaction. The angular acceleration of each particle was calculated from the orientation, as shown in Fig. 4.7. Using the values

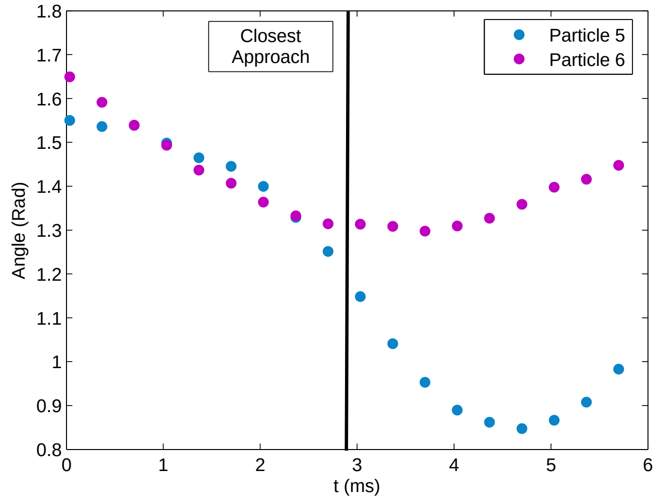

Figure 4.7: Orientation angle verses time for P5 and P6 with the solid line showing the time of closest approach.

of charge and external electric field found in the previous step, and substituting these values into Eq. (4.5), the electric dipole moments for each of the dust grains were found to be $|\vec{p_5}| = 0.3 \times 10^{-20}$ Cm and $|\vec{p_6}| = 2.8 \times 10^{-20}$ Cm with an estimated uncertainty of $\pm$ 20%.

Using reconstructed 3D models of P5 consisting of eight monomers, Fig. 4.8(a), and P6 consisting of sixteen monomers in OML_LOS, charges and electric dipole moments of aggregates were calculated as $q_5 = -0.58 \times 10^{-14}$ C and $q_2 = -0.83 \times 10^{-14}$ C with corresponding components of dipole moments $|\vec{p_5}| = 0.37 \times 10^{-20}$ Cm and $|\vec{p_6}| = 2.7 \times 10^{-20}$ Cm. These values are in good agreement with the values derived from experiment. The minor differences seen are assumed to arise from the sensitivity of the OML_LOS code to the number of monomers and their exact orientation in the constructed 3D aggregates.

Note that the values derived from (OML_LOS) code are sensitive to the number of monomers and their exact arrangements used to build up the 3D structure of the aggregates. Fig. 4.8 shows a 3D model of aggregate P5 (shown in Fig. 4.3) modified by displacing or removing one or two of the monomers at different positions

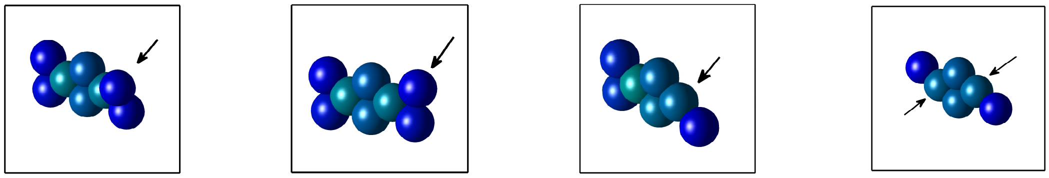

(a) (b) (c) (d)

Figure 4.8: Proposed structure of aggregate P5 consisting of different numbers of monomers. (a,b) eight monomers with the location of displaced monomer indicated by an arrow, (c) seven monomers, and (d) six monomers, with the locations of the removed monomers indicated by arrows.

to illustrate the resulting change in charge and electric dipole moment, listed in Table 4.1.

Aggregate	q (10^{-14} C)	$\mid \vec{p} \mid$ (10^{-20} Cm)	$\mid \vec{p_r} \mid$ (10^{-20} Cm)
(a)	-0.58	0.37	0.37
(b)	-0.58	0.24	0.23
(c)	-0.55	0.89	0.79
(d)	-0.52	0.30	0.23

Table 4.1: Electric charge, q, total dipole moment, $\mid \vec{p} \mid$, and projection of dipole moment in the image plane, $\mid \vec{p_r} \mid$, of aggregates in Fig. 4.8 derived from OML_LOS

The accuracy of the derived values are tested by modeling the dynamics of the interaction in $Aggregate-Builder$. Fig. 4.9 compares the observed and the modeled interaction where charges and electric dipoles are those predicted by OML_LOS, using the model for P5 shown in Fig. 4(a). The trajectory and orientation of the modeled aggregates are quite similar to the observed interaction, with a small deviation in rotation of aggregates after passing the points of closest approach. While the charge and electric dipole moments were taken to be constant in the simulation, the aggregate charge can change during the interaction, either due to induced dipole moments (the surface of the aggregates are coated with gold, a conductor) or by the proximity of the other grain altering the charging currents. The forces arising from the external electric fields are quite small compared to the screened Coulomb interaction between the aggregates and have a small impact on the particles' trajectories, the

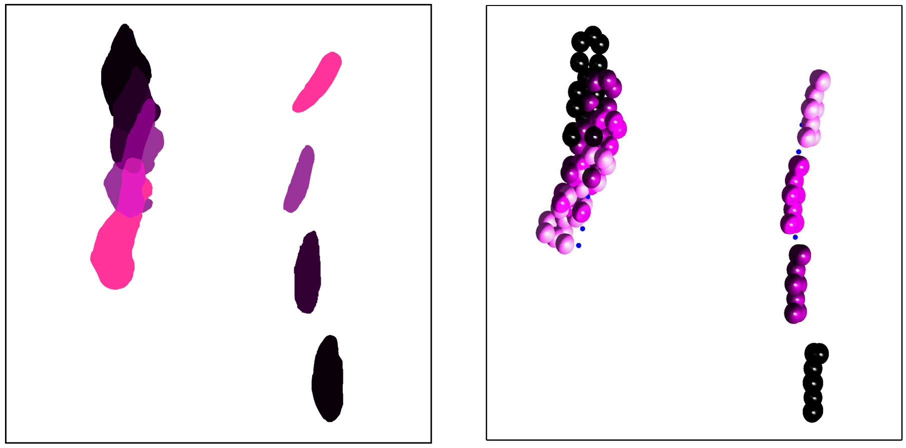

(a)

(b)

Figure 4.9: A superposition of four frames showing the interactions between two aggregates from (a) experimental data with similar color of aggregates in each frame and (b) simulation using *Aggregate_Builder* code with similar color of aggregates at each time step. Not all monomers are visible.

dynamics are quite sensitive to the interacting particles' charges and electric dipole moments as well as their initial positions, velocities and orientations. In Fig. 4.10, the trajectories and orientations found using the models for P5 depicted in Figs. 4.8(b-d) are shown for comparison. A smaller dipole moment due to the displacement of a single monomer (Fig. 4.8(b)) (though within the error bounds of the experimental value) results in an under rotation of P5 (Fig. 9(a)). Removing a monomer entirely (Fig. 4.8(c)) increases the charge-to-mass ratio of P5, but not enough that the trajectory is strongly affected. However, the large dipole moment results in an over-rotation (Fig. 4.10(b)). Removing two monomers (Fig. 4.8(a)) makes the charge-to-mass ratio small enough that the grain's trajectory deviates substantially from the observed motion.

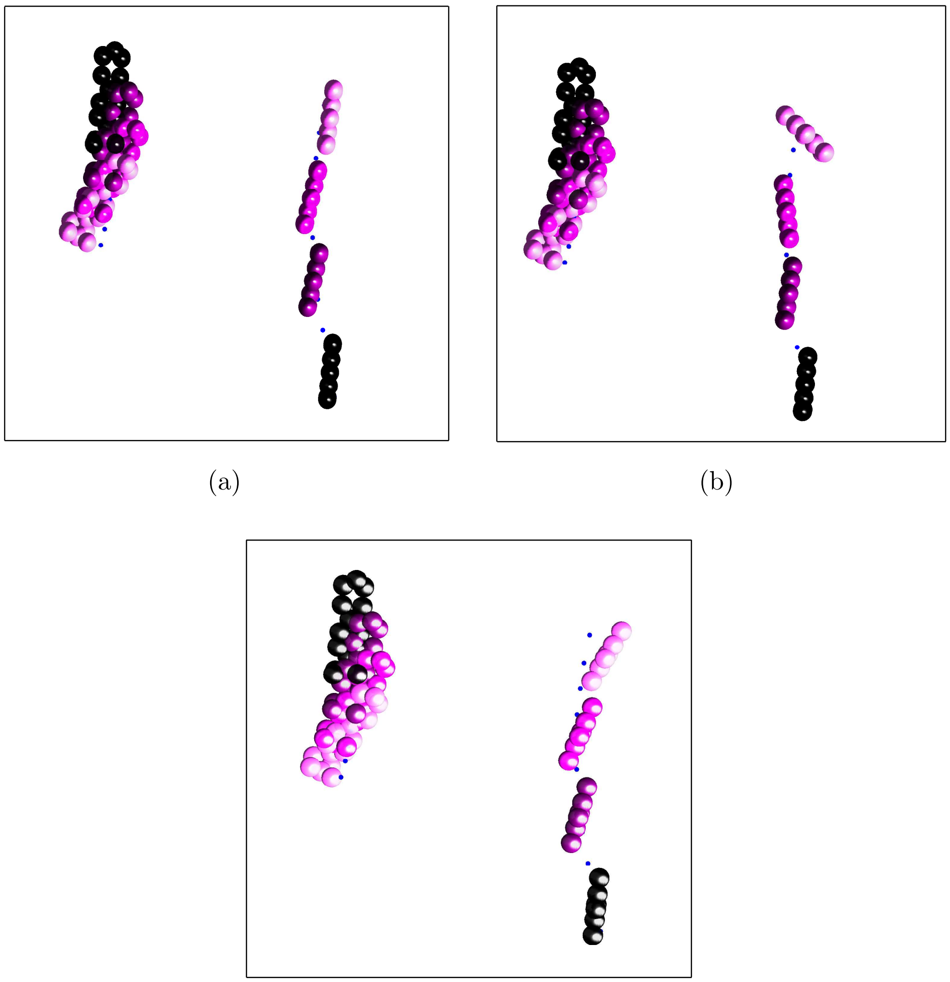

(a) (b) (c)

Figure 4.10: A superposition of four frames from *Aggregate_Builder* code with similar color of aggregates at each time, showing interaction of P6 with (a,b,c) corresponding aggregate in Fig. 4.8(b,c,d) respectively, (d) P5 with initial velocity half of the measured value from experiment.

CHAPTER FIVE

Charge on Dust Particles in a Vertical Particle Chain

In laboratory RF plasmas, dust particles tend to self-organize in ordered structures, such as plasma crystal. These particles are trapped in the sheath of the plasma, above the lower electrode where an inhomogeneous electric field in the vertical direction levitates the particles against gravity as explained in Chapter Three [81, 82, 83]. Placing a glass box on the lower electrode increases the horizontal confinement, allowing single or multiple vertical chains to be formed [71, 72, 84, 85, 86].

The stability of the aligned structures are not easily explained on the basis of a repulsive potential between particles and appears to be dependent on the balance between an attractive ion wakefield and the repulsive screening Coulomb potential [69, 87]. In the region of the sheath-plasma interface above the lower electrode, positive ions accelerate downward toward the lower electrode. As illustrated in Fig. 5.1, the ion flow, deflected by the negatively charged grains, leads to the formation of excess positive space charge just below the negatively charged dust grains levitated in the sheath [88]. Based on numerical calculations, the positive space charge becomes weaker for the downstream grains since a significant fraction of ions has been deflected by upstream grains, so that the direction of motion is no longer along the direction of unperturbed ion flow but makes an angle with it [31]. In addition, the downstream particles become less charged, resulting in a smaller electrostatic lens to focus the ions downstream [89].

In order to understand the dynamics of aligned structures, it is necessary to have an understanding of charging of the particles in such arrangements. Charging of a single particle in the presence of the ion flow has been studied analytically by assuming a large population of trapped ions around the negatively charged dust grain, which makes it possible for the ion cloud to become polarized thus shielding the

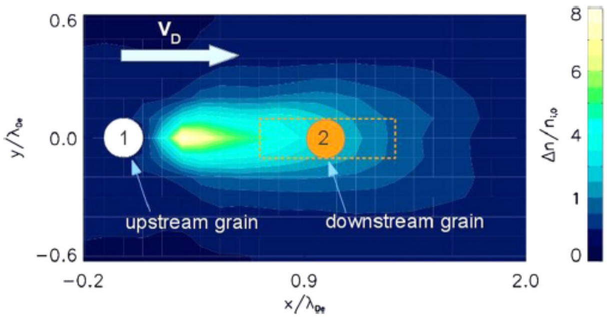

Figure 5.1: An illustration of a two particle chain aligned with the direction of an ion flow streaming from left to right. A positive space charge is formed below the upstream particle. In the simulation the downstream particle's position can vary in the region shown as a dashed box. Figure adapted from [31].

grain from electric fields and possibly leading to a van der Waals attractive force [90]. Understanding the dynamics of two or more particles is also complicated. In previous works the dynamics of two vertically aligned particles have been studied experimentally by analyzing the particle trajectories [83, 91, 92] and investigated numerically for the two vertically aligned dust particles in a flowing plasma [31, 92, 93]. In [31], the dynamics of three aligned particles was studied numerically by adding a third particle below the two aligned particles and calculating the forces acting on it.

The complex structure of multiple particles, such as a long chain, makes it hard to quantify the charge distribution on the dust particles as well as the positive space charges formed as a result of the ion flow. In this chapter, the dynamics of multiple dust particles in experimentally observed vertically aligned particle chains are analyzed numerically using a model based on the ion flow and the formation of positive space charges below the top particles in the chain. The best values for charges on the particles, as well as the positive space charges and their positions, are derived and these results are compared with previous studies.

5.1 Experiment

A single vertical dust particle chain is formed at the center of the glass box with the RF power set at $6.5W$. By slowly decreasing the RF power, the lowest particle

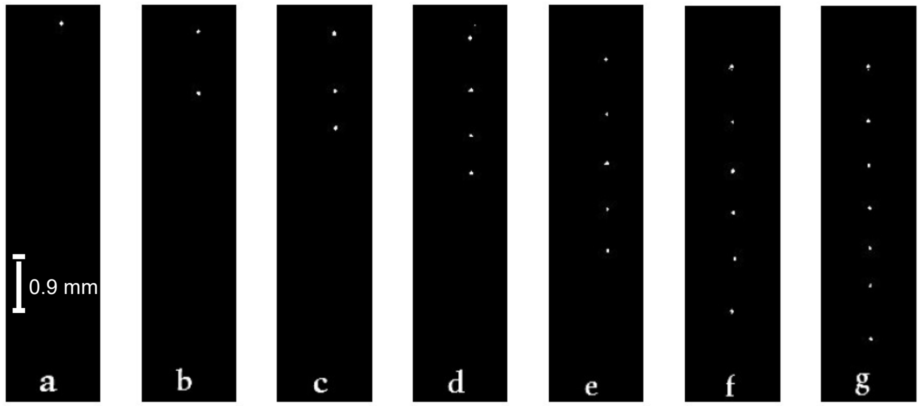

Figure 5.2: The vertical alignment of single-particle to seven-particle chains, left to right. Vertical position of dust particles are measured from this data.

in the chain is removed, leaving a chain consisting of six particles. The RF voltage is then returned to its original magnitude and the particle positions are recorded. By lowering the power further, the length of the chain is shortened by removing the lowest particle from the chain [94] and a vertical chain consisting of five, four, three, two and one particles can be formed respectively as shown in Fig. 5.2. In each step, the power is returned back to its original setting and the particle alignment is imaged using the high speed camera.

5.2 Analysis

In order to study the charging of different particle arrangements in a flowing plasma, a model is constructed based on the formation of a positive space charge below the particles in a chain as a result of the ion flow. The positive space charge becomes weaker for the downstream grains for two reasons: first, the downstream particles become less charged, resulting in a smaller electrostatic lens [31], and second, the velocity of the ions increases as they approach the lower electrode, resulting in larger momentum, which makes it harder for negatively charged dust particles to affect the ion trajectory to form a positive space charge. Therefore, a positive space charge is assumed to exist only beneath the two top particles in a chain. Fig. 5.3

shows a schematic of the model which is used to study the charging of the particles in a vertical chain.

In the experiment, as described in Chapter Three, gravity pushes the grains toward the lower electrode, while within the sheath a strong vertical electric field arising from the negatively charged lower electrode pushes them upward. The interaction force between negatively charged dust grains is a shielded Coulomb interaction, as has been considered in many previous calculations [49, 95, 96]. For simplicity, the electric force arising from the positive space charges is assumed to be a Coulomb electric force which attracts the downstream negatively charged dust particles.

Due to the experimental geometry and the vertical structure of particles, only a 1D set of equations is present. For the ith particle in a chain consisting of n particles, the total force, $\vec{F}_{tot_i}$, is

$$\vec{F}_{tot_i} = \vec{F}_{G_i} + \vec{F}_{z_i} + \vec{F}_{int_i} \tag{5.1}$$

where $\vec{F}_{G_i} = -m_i g\hat{z} = -mg\hat{z}$ is the gravitational force on the ith dust particle with mass $m_i = m$, $\vec{F}_{z_i}$ is the electrostatic force arising from the lower electrode and $\vec{F}_{int_i}$ is the electrostatic interaction force between the particles.

It is assumed that the lower electrode, with a geometry of a circular disk of radius R, carries a uniform charge density σ, which results in an electric field force

$$\vec{F}_{z_i} = q_i(\frac{\sigma}{2\epsilon_0}[1 - \frac{z_i}{(z_i^2 + R^2)^{\frac{1}{2}}}]) \tag{5.2}$$

where q_i is the charge on the ith particle at vertical position z_i. To first order, this gives an electric field which is linear in z, which is a common assumption made for the sheath electric field [49, 79].

The particle-particle interaction force, $\vec{F}_{int_i}$, is the electrostatic force on the ith particle in the chain arising from the rest of the charged dust particles as well as the assumed positive space charges, as given by the following equation

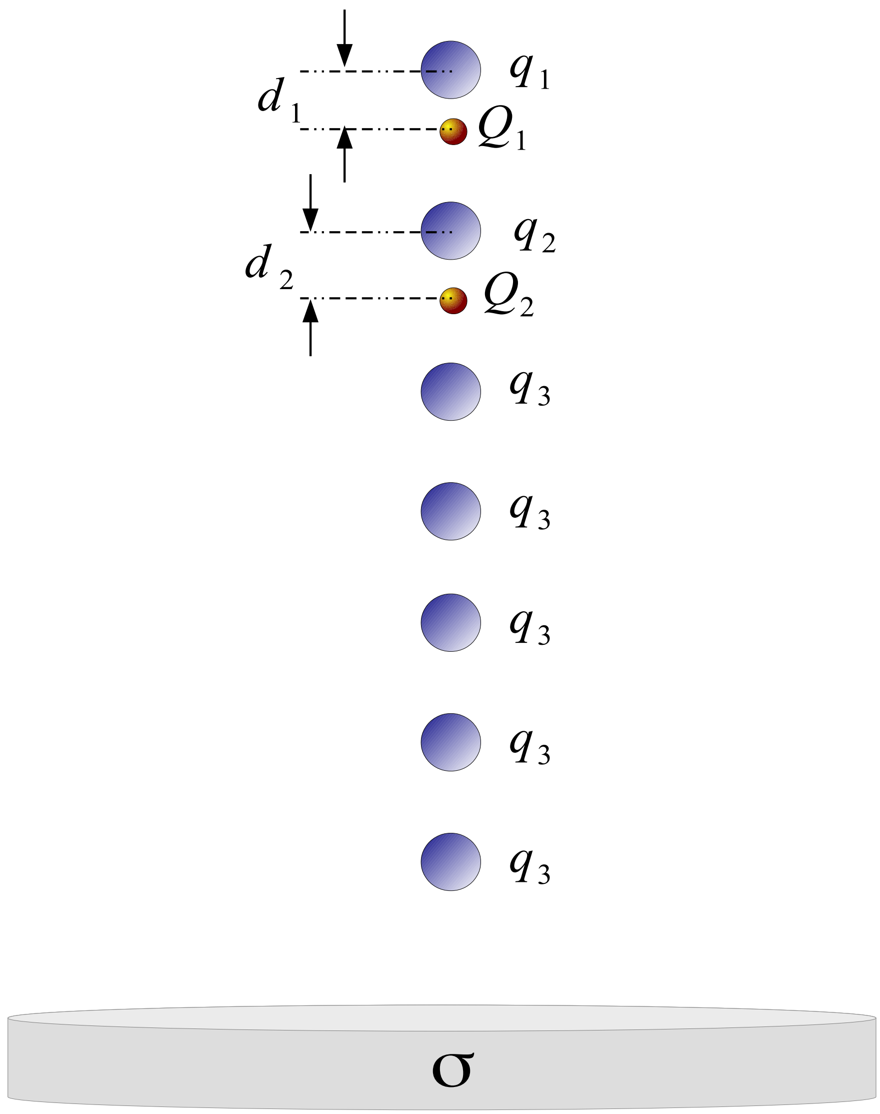

Figure 5.3: A schematic of the model used for studying charging of the dust particles in vertical structures in a flowing plasma. The positive space charges are formed below the two upstream particles. The top particle carries a charge q_1 with a positive space charge Q_1 below it at distance d_1. The second dust particle carries the charge q_2 with a positive space charge, Q_2, at distance d_2 below it. The remaining particles carry the same charge q_3. The dust particle chain is formed in the sheath above the lower electrode, which is assumed to have a uniform charge distribution σ.

$$\vec{F}_{int_i} = -\frac{q_i}{4\pi\epsilon_0}\Sigma_{j=1}^{n-1}[\frac{q_j}{z_{ij}}(\frac{1}{z_{ij}}+\frac{1}{\lambda})\exp(\frac{-z_{ij}}{\lambda})\frac{\vec{z_{ij}}}{z_{ij}}] + \frac{q_i}{4\pi\epsilon_0}\Sigma_{k=1}^{2} q_k \frac{\vec{z_{ik}}}{{z_{ik}}^3} \qquad (5.3)$$

where $z_{ij} =\mid z_i - z_j \mid$, $\vec{z_{ij}} = (\vec{z_i} - \vec{z_j})$, λ is the screening length (assumed to be constant for all the dust particles), and n is the number of dust particles. In the first part of the equation, the interaction force arising from the jth dust particle is given while the second part represents the electrostatic force due to the kth assumed positive space charges. As the space charges result from the focusing of the ions in the plasma, the additional shielding due to other ions in the plasma is not considered in calculating the interaction force.

5.3 Results

Solving for for the charge on particles plus two positive space charges, with d_i, λ and σ as unknowns requires a set of $n+6$ equations. Since only one equation of the form of Eq. 5.4 can be obtained for each particle, some simplifying assumptions must be made.

As a first step, it is assumed that all the particles below the top two particles have the same charge, q_3. This brings the number of unknowns to nine, and therefore a chain of seven particles in addition to two space charges provides the necessary number of equations.

The particle chains observed in this experiment are assumed to be stable structures with $\vec{F}_{tot} = 0$. The vertical position of each particle, z_i, is obtained from experiment as shown in Fig. 5.2, and these values are substituted into Eqs. 5.2 and 5.3.

A numerical method is used to solve the set of equations by setting two initial values for each variable. The actual value of each variable is assumed to lie within this range, and each variable is adjusted until all of the equations are satisfied within an allowed tolerance of error, ϵ,

$$|F_{tot_i}| < \epsilon \qquad\qquad (i = 1 \textit{ to } 7). \qquad (5.4)$$

variable	value
q_1	-5.54 (10^{-15} C)
q_2	-4.38 (10^{-15} C)
q_3	-4.16 (10^{-15} C)
Q_1	+1.01 (10^{-15} C)
Q_2	+0.46 (10^{-15} C)
d_1	180 (μ m)
d_2	300 (μ m)
λ	7.05 (10^{-4} m)
σ	-2.88 (10^{-8} $\frac{C}{m^2}$)

Table 5.1: Results from solving the system of equations of motion for a seven particle chain with error tolerance $\epsilon = \frac{mg}{50}$, where m is the mass of the dust particles.

The values are provided in Table 5.1 for $\epsilon = \frac{mg}{50}$. From Table 5.1, $q_2 = 0.80\, q_1$, which is consistent with previous experimental observation where the downstream particle is measured to have a charge of 78% of the upstream particle, i.e. $q_2/q_1 = 0.78$ [97]. The positive space charge Q_1 is found to be $Q_1 = 0.18\, q_1$ which is in agreement with the numerically predicted value for a positive space charge of 15% of the charge on the upstream particle [31]. In addition $d_1 = 18\%$ of the inter-particle spacing, which supports the former results for position of the positive space below the top particle [93, 92]. Note that $Q_2 = 0.08 q_1$ also provides support for the assumption that smaller positive space charges exist for down-stream particles, as considered in the former studies as well [31]. The screening length is found to be $\lambda \approx 0.9\delta z$ where δz is the average spacing between the dust particles. This value is in agreement with the calculations for stable aligned structures using a dynamically screened Coulomb interaction between dust grains in a chain [98].

This set of solutions is derived for the case where the third through seventh down-stream particles all carry the same charge. In the next step, using the same algorithm, the charges on the down-stream particles are allowed to differ by defining two initial values for each of these charges and allowing them to take different values. This allows the magnitude of error to become as small as $\epsilon = \frac{mg}{10^4}$.

This numerical method is then used to estimate the charges on each particle in shorter chains, where again the ion flow is assumed to create positive space charges only below the the top two particles. In the calculations, none of the parameters are set to be constant, but are allowed to vary within a narrow range about the best-fit values calculated for the previous iteration. The results for the magnitude of the charges on each particle in chains of different length are provided in Fig. 5.4.

Although there is no way to prove that these are the unique solutions to the systems of equations, these results are compatible with previous numerical and experimental studies. For instance, for the two particles in a chain, the charge on the down-stream particle is found to be about 85% of the charge on the top particle, comparable to the results derived in [92] by measuring the attractive force between two aligned dust particles. Moreover, the top positive space charge is found to be 16% of the charge on the top particle with its position 17% of the spacing between the two dust particles, results which are in good agreement with previous studies where the stability of aligned structures has been studied by calculating the forces on the dust particles in a flowing plasma [93]. In addition, for the three particle chain, the middle particle has the smallest charge of the three particles in the chain, about 84% of the top particle's charge, while the lowest particle charge is 86% of that of the top particle. A similar relation between the charges for a three particle chain is predicted in [31] using a numerical method in a flowing plasma.

In general, the charge on the dust particles in a chain decreases from top to bottom as expected, since the number density of electrons decreases relative to that for ions in the plasma sheath as the boundary (lower electrode) is approached. As shown in Fig. 5.4, in the longer chains ($N = 4 - 7$), the charge differences between the lower particles is smaller than that for the top particles, indicating a uniform plasma condition in a small sheath region between $4 \leq z \leq 7mm$. Also notable is the fact that in the three to five particle chains, the charge of the lowest particle is greater

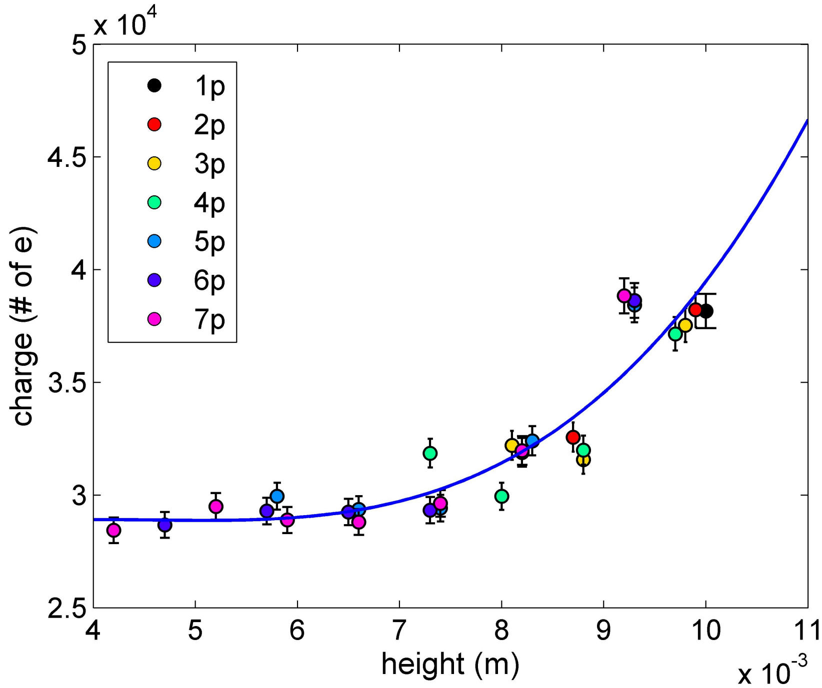

Figure 5.4: Charge distribution on the dust particles in particle chains consisting of different number of particles from one to seven. The horizontal axis represents the vertical position of a dust particle, with the charge of the dust particles shown on the vertical axis. The charge depends on the position of the dust in the sheath as well as the relative dust particle distribution. The solid line represents the best fit line using a third degree polynomial.

than that of the particle just above it. The reason for this could be the shadowing effect [99, 100], since the lower particle is just shielded in one direction by the upper particles while the particle above it is shielded from two directions.

The vertical electric field at the position of each particle in the chain is also calculated. As all the chains are observed at the same plasma condition, one may expect to find similar electric fields at the same heights. As shown in Fig. 5.5, the magnitude of the electric field is found to be linear, providing a check on the self-consistency of both the numerical method and derived solutions in this work. The vertical electric field is similar to the magnitude of the electric field determined by a different experimental method with similar plasma conditions [49] and numerical calculations for the sheath without a glass box present [101].

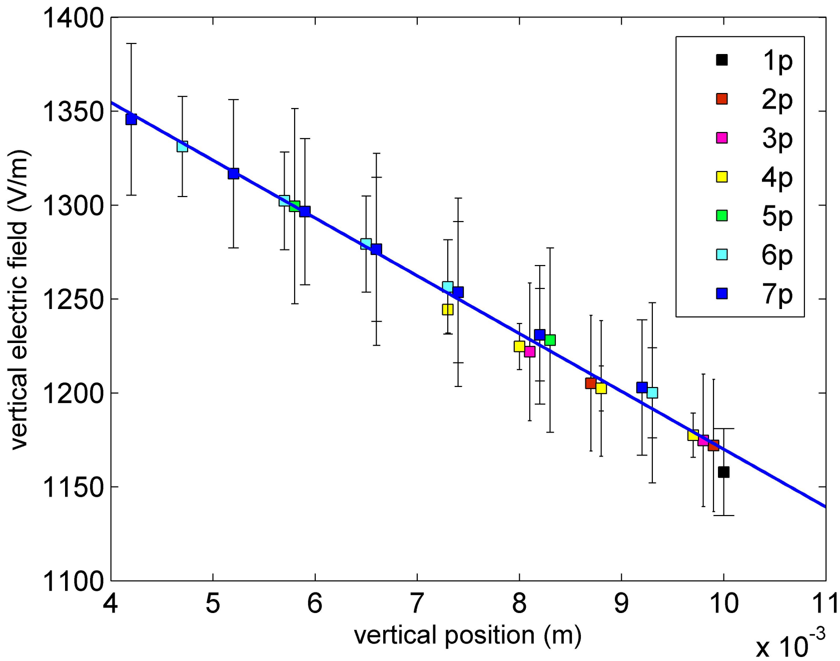

Figure 5.5: Vertical electric field determined at different particle positions for several chains at same plasma condition. The electric field is found to be linear in this small region of the sheath. The error bars are calculated from the electric field relation considering the lower and upper values for the derived σ.

CHAPTER SIX

Electric Charge and Dipole of Dust Aggregates in the Presence of Ion Flow

As discussed previously in Chapter Two, in the sheath of dusty plasmas, ions accelerate toward the boundary of the plasma. As a result, dust grains inside the sheath experience ions streaming toward them from one direction. This ion flow has an impact on charging of the dust. This chapter describes an algorithm which may be used to estimate the dipole moment on charged dust grains, including aggregates, by a modified version of the OML_LOS code.

6.1 Numerical Analysis

One of the dominant charging processes is collection of ions and electrons by the surface of the dust, which can be modeled by OML theory as described in Section 2.3.1. In the plasma sheath, where ions are accelerated towards the boundary, the velocity distribution of the ions is no longer Maxwellian, but is instead described by Eq. 2.24. Rewriting Eq. 3.1 for J_j, the flux of the jth plasma species, toward the surface of the dust, we have

$$J_j = n_j q_j \int\int\int f_j(v_j) v_{nj} d^3 v_j \tag{5.1}$$

in which f_j is assumed to be a Maxwellian velocity distribution function. In the presence of ion flow, streaming with a constant velocity $\vec{v_d}$, considering a Maxwellian distribution function for velocity as given in Eq. 2.20 for electrons and Eq. 2.24 for ions substitute in Eq. 5.1, the electron and ion flux toward the surface of the dust are respectively as follows

$$J_e = n_e (\frac{m_e}{2\pi k_B T_e})^{3/2} \int\int\int \exp(-\frac{m_e v_e^2}{2k_B T_e} - \frac{q_e \phi_s}{k_B T_e}) v_{ne} d^3 v_e \tag{5.2}$$

and

$$J_i = n_i(\frac{m_i}{2\pi k_B T_i})^{3/2} \int\int\int \exp(-\frac{m_i(\vec{v}_i - \vec{v}_d)^2}{2k_B T_i} - \frac{q_i \phi_s}{k_B T_i}) v_{ni} d^3 v_i. \quad (5.3)$$

For a single spherical dust grain, analytical solutions to these equations are provided in detail in Section 2.3.2. Solving Eq. 5.3 for a dust aggregate with a complex structure, is more difficult. For a dust aggregate in a uniform plasma condition, the charging may be addressed through the numerical model, OML_LOS which presented in detail in Section 3.3. We can modify this numerical simulation to calculate the charging of a dust aggregate in the presence of ion flow.

Considering Fig. 6.1, at a given point on the surface of the dust, an ion hits the surface with a velocity $\vec{v}_i$. The ion streaming velocity, $\vec{v}_d$, is assumed to be in the vertical direction, meaning the streaming ions hit the surface from the top. The spatial coordinate system xyz is chosen such that the origin lies at the center of mass of the dust grain, the local coordinate system $x'y'z'$ centered at the point of impact and oriented such that z' is along the surface normal. The orientation of the x' and y' axes are chosen such that the projection of the ion streaming velocity, $\vec{v}_d$, is along the x' axis so that the azimuthal angle is zero. Thus in $x'y'z'$ coordinate system, $\vec{v}_d$ and $\vec{v}$ are given as follows

$$\vec{v}_d = v_d \sin(\theta)\hat{x}' + v_d \cos(\theta)\hat{z}', \quad (5.4)$$

and

$$\vec{v} = v \sin(\alpha)\cos(\beta)\hat{x}' + v \sin(\alpha)\sin(\beta)\hat{y}' + v \cos(\alpha)\hat{z}'. \quad (5.5)$$

where α and β are polar and azimuthal angles in $x'y'z'$ coordinate system. Therefore,

$$\vec{v} \cdot \vec{v}_d = v v_d(\cos(\alpha)\cos(\theta) + \sin(\alpha)\cos(\beta)\sin(\theta)). \quad (5.6)$$

therefore

$$(\vec{v} - \vec{v}_d)^2 = v^2 + v_d^2 - 2\vec{v}\cdot\vec{v}_d = v^2 + v_d^2 - 2v v_d(\cos(\alpha)\cos(\theta) + \sin(\alpha)\cos(\beta)\sin(\theta)). \quad (5.7)$$

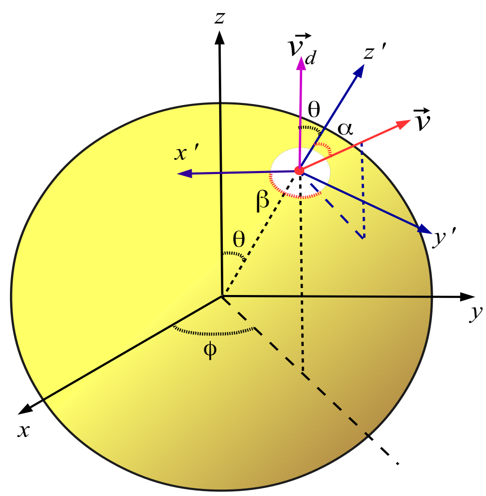

Figure 6.1: A schematic of a spherical dust particle grain with θ and ϕ representing the angles in the spherical coordinate system xyz with origin at the center of the dust. The ion flow is along $\vec{v_d}$ and plasma particles hit the surface with velocity directed along $\vec{v}$. The angles α and β in the $x'y'z'$ coordinate system with origin at the point of contact.

Substituting Eq. 5.7 into Eq. 5.3 gives

$$J_i = n_i(\frac{m_i}{2\pi k_B T_i})^{3/2} \int\int\int v_i \cos(\alpha)$$
$$\exp(-\frac{m_i(v^2 + v_d^2 - 2vv_d(\cos(\alpha)\cos(\theta) + \sin(\alpha)\cos(\beta)\sin(\theta)))}{2k_B T_i})v_i^2 \sin(\alpha) dv_i d\alpha d\beta. \tag{5.8}$$

In order to solve this integral numerically, there are few points we have to consider: first, since ion streaming is in one direction toward the dust surface, only one side of the dust is assumed to be affected by ion flow. Therefore, considering Fig. 6.1, only the top side of the dust is affected by ion flow and $v_d = 0$ for $\alpha = \pi/2 \to \pi$. Second, the upper limit of the velocity integral is ∞ as discussed in Section 2.3.2. Although there is a wide distribution of velocities, 90% of the velocities are between $1/2\bar{v}_{av}$ and $2\bar{v}_{av}$ [102], where $\bar{v}_{av}$ is the average velocity, and using the following relation

$$\bar{v_i} = (\frac{m_i}{2\pi k_B T_i})^{3/2} 4\pi \int_0^\infty v^3 \exp(-\frac{m_i(v_i - v_d)^2}{2k_B T_i}) \tag{5.9}$$

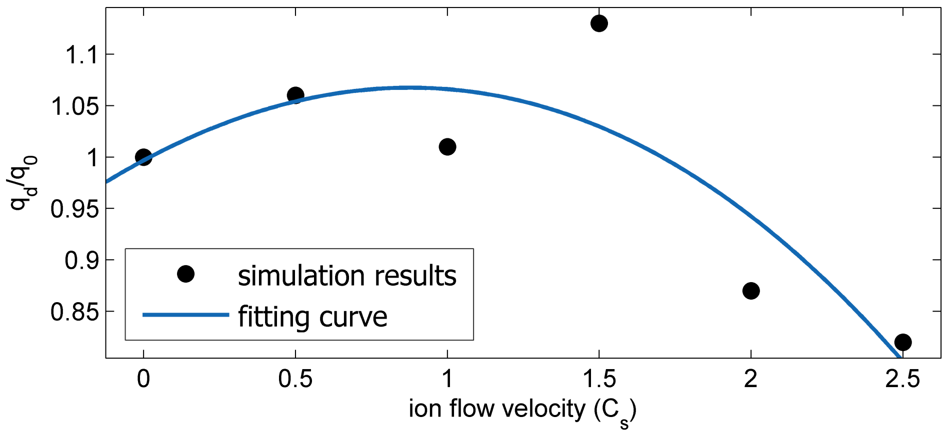

Figure 6.2: A representation of the equilibrium charge on the dust grains at different flow velocities.

the average ion velocity is derived as follows

$$\bar{v_i} = (\frac{8k_BT_i}{m_i\pi})^{1/2} + \frac{2m_i}{k_BT_i}v_d^3 + 3\pi v_d + 3v_d\sqrt{\frac{2m_i}{k_BT_i}}, \tag{5.10}$$

Finally, for the dust aggregates we have to consider the open and blocked directions for plasma particles hitting the surface of the dust at each point as discussed in section 2.5. Taking into account all of these considerations and using the same method as discussed for the OML_LOS code, by considering a uniform distribution of points on the surface of dust the electric charge and dipole moment of dust is calculated using the following relation for ion flux

$$J_i = n_i(\frac{m_i}{2\pi k_BT_i})^{3/2}\Sigma_{v_i}\Sigma_\alpha\Sigma_\beta v_i\cos(\alpha)$$
$$\exp(-\frac{m_i(v^2+v_d^2-2vv_d(\cos(\alpha)\cos(\theta)+\sin(\alpha)\cos(\beta)\sin(\theta)))}{2k_BT_i})v_i^2\sin(\alpha)\delta v_i\delta\alpha\delta\beta. \tag{5.11}$$

where the sum is taken along the unblocked directions defined by α and β.

6.2 Results

For a spherical dust grain in the presence of ion flow, the charging of the dust is studied for different ion flow velocities. Fig. 6.2 shows the charge on a single dust as

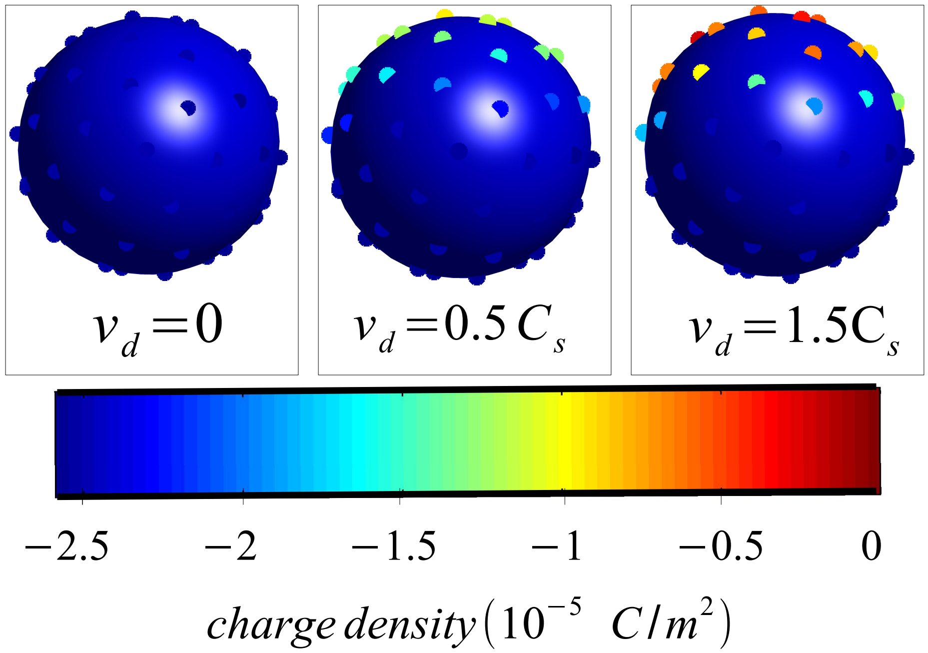

Figure 6.3: A schematic of three spherical dust particles in the presence of ion flow at different flow velocities from simulation. The color scale shows the charge density of the surface of the dust.

a function of ion flow velocity. The general trend of the graph is in agreement with previous results shown in Fig. 2.3. In order to visualize the charge distribution on the surface of the dust in the presence of ion flow, a comparison is made between a dust particle in a uniform plasma condition and two dust particles in the presence of ion flow at different flow velocities as shown in Fig. 6.3.

The charge on a dust aggregate with an irregular structure, composed of different size dust monomers in the presence of ion flow with a velocity $1C_s$ is also compared to the same dust aggregate in a uniform plasma condition as shown in Fig. 6.4. Both the total electric charge and vertical component of electric dipole moment of the dust aggregate are affected by the ion flow. While the electric charge of the aggregate in the presence of ion flow is only moderately increased by $\approx 7\%$ over the total charge in a uniform plasma, the vertical component of electric dipole moment is about 4.7 times larger than that in the uniform plasma condition.

6.3 Comparison With Experiment

Two experimental observations are presented and compared with the simulation. It is shown that the presented numerical method can explain some of the observations including charging of two particles in a vertical chain and attractive force between two negatively charged dust particles in the presence of ion flow.

6.3.1 Vertical Chain of Two Dust Particles

One of the interesting experimental observations in a laboratory dusty plasma experiment is formation of ordered structures such as dust particle chains in the sheath of the plasma. This problem was studied in Chapter Five in detail for one to seven particle chains, and it was shown that the dust particle just below the top particle in a vertical chain carries a charge smaller than that of the top particle. The same results are derived from the calculation of charge with ion flow for different flow velocities. These results are provided in Table 6.1. The charge on the lower particle is calculated to be $\approx 89\%$ to $\approx 97\%$ of the charge on the top particle for $v_d = 0.5C_s$ to $v_d = 1.5C_s$. The lower particle is blocked by the top particle in the flow direction, and as a result it does not experience the ion streaming effect.

v_0 (C_s)	q_{top} ($10^4 e$)	q_{lower} ($10^4 e$)
0	2.05	2.05
0.5	2.18	2.05
1	2.10	2.05
1.5	2.31	2.05

Table 6.1: A comparison between charging of the dust particles in a vertical two particle chain at different ion flow velocities.

6.3.2 Attractive Interaction Between Two Dust Particles

Another interesting observation in the dusty plasma experiments is the apparent attractive force between similarly charged dust particles. For a two-particle chain in an experiment similar to that presented in Chapter Five, the top particle is manipulated by laser light, pushing it from its equilibrium position. Fig. 6.5 shows the

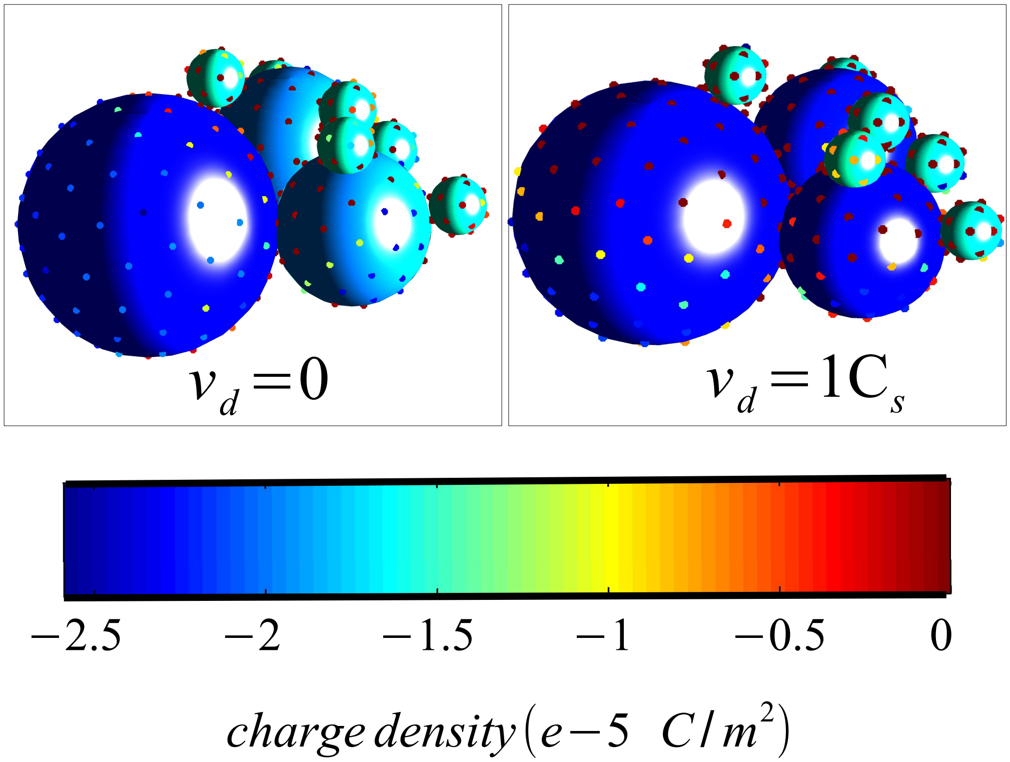

Figure 6.4: A dust aggregate with an irregular structure composed of spherical monomers of different sizes in the uniform plasma condition (left) and in the presence of ion flow (right) with the ion streaming velocity $v_d = 1C_s$ in the vertical direction.

superposition of two frames at times $t1$ and $t2$ with particle displacement indicated by arrows from $t1$ to $t2$. It is clear from the displacement that the lower particle is following the top particle, being attracted to it. This attraction can not be explained by repulsive Coulomb interaction between negatively charged dust particles. One of the propositions to explain this phenomena is that the attraction can be a result of dipole interaction between dust particles. Since the particles are in the plasma sheath, the particle have electric dipole moments which develop due the ion flow. Under specific conditions, this may explain the attractive force.

Examining the charge on the dust particles when the two dust particles are at the closest approach, the electric charge and vertical component of electric dipole moment of the two particles are almost the same and calculated to be respectively $q1 \approx q2 = -3.5(10^{-15}C)$ and $p1 \approx p2 = 5.8(10^{-21}Cm)(\hat{z})$.

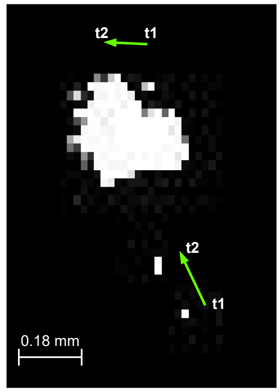

Figure 6.5: A superposition of two frames at times $t1$ and $t2$ showing the displacement of the two dust particles shown by arrows. The lower particle follows the top one as the top one is pushed to the left by the laser. The laser illumination on top particle is observed as a big blob.

In considering the horizontal motion of the upper particle, $P1$, we assume that the dominant forces acting on the dust particle are the mutual electrostatic forces between the grains. The neutral drag force is assumed to be negligible since the velocity of the particle is small, and the confinement force from the radial electric is also taken to be small since the particle position is almost at the center of the box. For $P1$, the force equation then becomes

$$F_{horizontal} = q1(\vec{E}_{q2} + \vec{E}_{p2}) \cdot \hat{x} \tag{5.12}$$

where for a spherical dust grain with radius $r_d = a$ [103],

$$E_{q2} = \frac{q2}{4\pi\epsilon_0 r}\frac{\exp(-\kappa(r-a))}{(1+\kappa a)}\hat{r}\cdot\hat{x} \tag{5.13}$$

and considering the shielding effect,

$$E_{p2} = \frac{p2\cos(\theta)}{4\pi\epsilon_0 r^2}\exp(-\kappa(r-a))\frac{3(1+\kappa r)}{\kappa^2 a^2 + 3\kappa a + 3}\hat{r}\cdot\hat{x} \tag{5.14}$$

where $\kappa = 1/\lambda_D$, θ is the polar angle as shown in Fig. 6.6, and r is the distance between the two dust particles at the closest approach, which is measured from experiment. From these equations, assuming $\lambda_D \approx 0.05mm \approx 10a$, the charge and

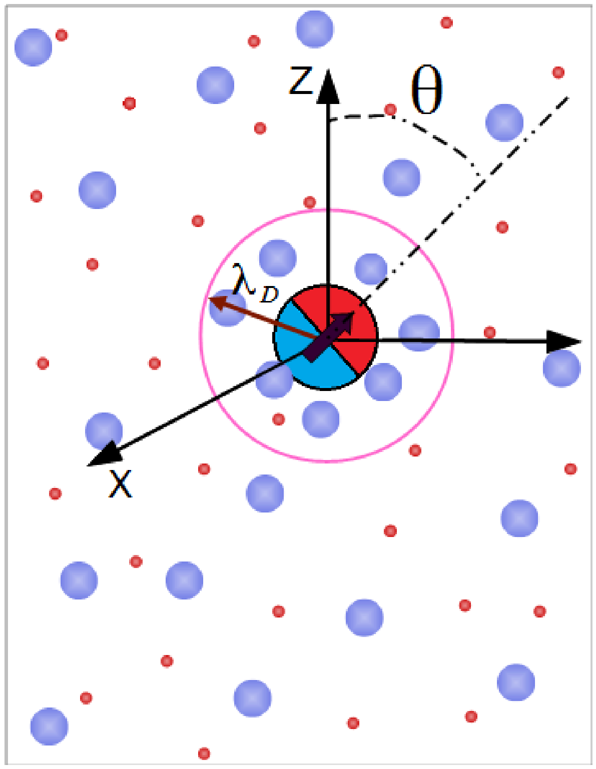

Figure 6.6: A schematic of a spherical charged particle carrying an electric charge as well as electric dipole moment with a polar angle θ. The electric charge and dipole moment of the dust are affected by shielding of ions.

dipole moment are found to be $-4.0(10^{-15}C)$ and $6.1(10^{-21}Cm)$. These results are in agreement with the numerical model and show that the dipole charge interaction could be a candidate for explaining the attractive force between charged particles in a flowing plasma.

CHAPTER SEVEN

Summary

Experimental and numerical methods to determine the electrostatic characteristics of dust grains in a plasma are presented. These measurements of the fundamental electrostatic properties, such as charge and dipole moment, are of importance in understanding the aggregation process, where the charge and electric dipole moment play a very important role in determining the evolution of the grain-size distribution, and in characterizing dust-plasma interactions, especially as micron-sized dust grains have been found to be very sensitive probes of the local plasma environment. Three specific cases were examined: I) electric charge and dipole moment of dust aggregates in a plasma assumed to be uniform, and II) charge on dust particles in a vertical particle chain and III) electric charge and dipole moment of dust aggregates in the presence of ion flow.

In most of the previous works where dipole moments are reported, aggregates were simplified to be treated as highly symmetric grains such as spherical, elliptical or cylindrical grains [31, 61, 68, 90, 104, 105, 106]. However, this study was designed to investigate dust aggregates with irregular, non-symmetric complex shapes in order to evaluate the electrostatic charge and dipole moment.

The electrostatic charges and dipole moments of observed aggregates from experiment were determined through analysis of the extracted particle trajectories and rotations and compared to the predictions of numerical models. The excellent agreement between experiment and simulation validates the choice of underlying assumptions. For the numerical models, these include the simplifying assumptions that ions and electrons trajectories only impact the aggregate surface along open lines of sight and stick at the point of impact, and that rotations of charged grains are induced by charge-dipole interactions. In deriving values from experiment, the assumptions made include neglecting the ion drag force, considering a screened Coulomb interaction between charged particles in order to calculate the force between them, and ignoring the gradient in E_z and E_r during the time of interaction for interacting pair particles.

Vertical particle chains composed of seven and fewer particles were formed in an RF argon discharge plasma by confining particles within a glass box placed on the lower electrode in order to increase the radial confinement. The flowing ions are assumed to create positive space charges under the two upstream particles. Treating a chain as a stable system with each particle at rest, the force balance is derived by considering all the forces acting on the particles. For a seven particle chain, by assuming that the value of charges on the third and lower particles in the chain are the same while the two top particles carry different charges, the system of equations is solved using a numerical method to give an estimation of the value of charges on the particles along with other unknown parameters. The relationship between the value of charges on the dust particles as well as the quantity of positive space charges and their positions are in good agreement with previous studies [90, 91, 92, 93, 107].

Using the same numerical method, by allowing the charges on the particles in each chain to take on different values, systems of equations are solved for chains of different lengths separately. For two and three particle chains, these results are compared with the previous numerical and experimental studies based on a flowing plasma model, with the results in agreement. For instance, for a two particle chain, the value of the charge on the lower particle is 85% of that on the top particle, similar to the value derived in [92]. For a three particle chain the middle particle carries the smallest charge among the three particles, as predicted in [31].

Charging of the dust aggregates in the presence of ion flow was investigated numerically and it was shown that the electric charge and dipole moment of dust are affected in the presence of ion the streaming. As the velocity of the flow increases the magnitude of charge initially increases but then decreases for flow velocities $v_d > 1.5C_s$. The component of the electric dipole moment along the ion flow is affected so that spherically symmetric dust particles form a dipole moment in the direction of the ion flow, while in the uniform plasma the electric dipole moment is almost zero.

It was shown that for a two particle chain formed along the flow direction the value of charge on the lower particle is smaller than that on the top particle for some of the ion flow velocities, in agreement with the previous numerical and experimental predictions. In addition the electric dipole moment produced on the dust particles in the presence of ion flow can possibly explain the attractive force between negatively charged particles as a result of the electric dipole interaction.

The first part of this experimental study is the first analysis of irregular aggregates consisting of spherical monomers which quantifies the dipole moment of individual aggregates. These measurements of the electrostatic charges and dipole moments are of importance in understanding the aggregation process in dynamic simulations studying dust agglomeration where the charge and electric dipole moment play a very important role and determining the evolution of the grain-size distribution. The second part of this experimental study is also the first analysis which quantifies the value of charges on particles in long vertical chains of particles experimentally and the results for short chains (one, two and three particle chains) are shown to be in agreement with previous numerical and experimental works. These measurements of the electric charges will be of use to better understand the ordered structures and also provide a better understanding of the models by which aligned structures are explained.

Finally, the electrostatic properties of the dust aggregates in the presence of ion flow were investigated numerically with the results in agreement with the previous numerical predictions. It was shown that for two particle chain formed in the flow direction, for some of the ion flow velocities the charge on the lower particle tends to be smaller than that on the upper particle. In addition the apparent attraction between two negatively charged particles may be explained by the electric dipole interaction between two dust particles. The improvement of the presented numerical model is left as a future work. This includes increasing the efficiency of the code so that the electrostatic properties for very large aggregates can be calculated in a reasonable time. In the experimental analysis of the interaction between dust aggregates, additional forces such as photophoretic and thermophoretic forces should also be considered as forces governing the dynamics of the dust. This may give interesting results about the possible dominant forces acting on the dust.

BIBLIOGRAPHY

[1] P. A. Sturrock, Plasma Physics: An Introduction to the Theory of Astrophysical, Geophysical and Laboratory Plasmas, Cambridge University Press (1994).

[2] P. K. Shukla, A survey of dusty plasma physics, Phys. Plasmas 8, 1791 (2001).

[3] I. Langmuir, Oscillations in Ionized Gases, Proc. Nat. Acad. Sci. 14, 627 (1928).

[4] L. Tonks and I. Langmuir, Oscillations in Ionized Gases, Phys. Rev. 33, 195 (1929).

[5] J. A. Broun, Trans. R. Soc.Edingburg 18, 401 (1848).

[6] J. A. Broun, Phil. Mag. (4th Series) 16, 81 (1858).

[7] W. N. Hess, The radiation belt and magnetosphere, Blaisdell Pub. Co. (1968).

[8] C. K. Goertz, Dusty plasmas in the solar system, Rev. Geophys. 27, 271 (1989).

[9] R.L. Merlino, Plasma Physics Applied 81, 73 (2006).

[10] F. Verheest, Waves in Dusty Space Plasmas, Kluver Academic Publishers (2000).

[11] A. L. Peratt, Astrophys. and Space Sci. 227, 97 (1995).

[12] P. K. Shukla and A. A. Mamun, Introduction to Dusty Plasma Physics, IOP Publishing, London (2002).

[13] H. Alfven, On the Origin of the Solar System, Oxford: Clarendon (1954).

[14] G. A. Wurden, A. J. Wurden, and I. M. Gladstone, Plasma Tails: Comets HaleBopp and Hyakutake. IEEE Trans. Plasma Sci. 27, 142 (1999).

[15] J. Glanz, A Dusty Road for Space Physics, Science 264, 28 (1994).

[16] U. de Angelis, The physics of dusty plasmas, Phys. Scripta 45, 465 (1992).

[17] B. A. Smith et al., Encounter with Saturn-Voyager 1 imaging science results, Science 212, 163 (1981).

[18] B. A. Smith et al., A new look at the Saturn system - the Voyager 2 images, Science 215, 504 (1982).

[19] M. E. Ockert, J. N. Cuzzi, C. C. Porco, and T. V. Johnson, Uranian ring photometry: results form Voyager 2. J. Geophys. Res. 92(14), 969 (1987).

[20] B. T. Draine, Annu. Rev. Astron. Astr. 41, 241 (2003).

[21] M. A. Lieberman and A. J. Lichtenberg, Principles of Plasma Discharges and Materials Processing, John Wiley AND Sons, Inc (2005).

[22] H. Rothermel, T. Hagl, G. E. Morfill, M. H. Thoma, and H. M. Thomas, Phys. Rev. Lett. 89, 175001 (2002).

[23] F. F. Chen, R. H. Huddlestone, and S. L. Leonard, Electric Probes in Plasma Diagnostic Techniques, Academic Press. New York (1965).

[24] H. M. Mott-Smith and I. Langmuir, Phys. Rev. 28, 727 (1926).

[25] I. B. Bernstein and I. N. Rabinowitz, Phys. Fluids 2, 112 (1959).

[26] F. F. Chen, Plasma Phys. 7, 47 (1965).

[27] J. E. Allen, Phys. Scripta 45, 497 (1992).

[28] P. K. Shukla and A. A. Mamun, Introduction to Dusty Plasma Physics, IOP Publishing, London (2002).

[29] A. Melzer, and J. Goree, Fundamentals of Dusty Plasmas, WILEYVCH Verlag GmbH & Co. KGaA, Weinheim, Germany (2008).

[30] M. S. Sodha and S. Guha In Advances in Plasma Physics, edited by A. Simon and W. B. Thompson Inter-science, New York, 4, 219 (1971).

[31] W. J. Miloch, and D. Block, Phys. Plasmas 19, 123703 (2012).

[32] G. Lapenta, Phys. Plasmas 6, 1442 (1999).

[33] A. V. Ivlev, G. Morfill, and V. E. Fortov, Phys. Plasmas 6, 1415 (1999).

[34] N. Meyer-Vernet, Astronom. Astrophys. 105, 98 (1982).

[35] V.W. Chow, D. A. Mendis, and M. Rosenberg, IEEE Trans. Plasma Sci. 22, 179 (1994).

[36] C. K. Goertz, Dusty plasma in the solar system, Rev. Geophys. 27, 271 (1989).

[37] L. S. Matthews and T. W. Hyde, IEEE Trans. Plasma Sci. 36, 310 (2008).

[38] M. Rosenberg, J. Vac. Sci. Technol. A 14, 631 (1996).

[39] T. G. Northrop and T. J. Birmingham, Planet. Space Sci. 38, 319 (1990).

[40] M. S. Barnes , J. H. Keller, J. C. Forster, J. A. O'Neill, and D. Keith. Coultas, Phys. Rev. Lett. 68, 313 (1992).

[41] M. D. Kilgore, J. E. Daugherty, R. K. Porteous, and D. B. Graves. J. Appl. Phys. 73, 7195 (1993).

[42] X. Chen, J. Phys. D: Appl. Phys. 29, 995 (1996).

[43] C. Zafiu, A. Melzer, and A. Piel, Phys. Plasmas 10, 1278 (2003).

[44] P. S. Epstein, Phys. Rev. 23, 710 (1924).

[45] B. Liu, J. Goree, V. Nosenko, and L. Boufendi, Phys. Plasmas 10, 9 (2003).

[46] H. Vestner and L. Waldmann, Physica 86A, 303 (1977).

[47] G. M. Jellum, J. E. Daugherty, and D. B. Graves, J. Appl. Phys. 69, 6923 (1991).

[48] V. Land, B. Smith, L. S. Matthews, and T. Hyde, IEEE Transactions on Plasma Science, 38(4), 768 (2010).

[49] R. Yousefi, A. B. Davis, J. C. Reyes, L. S. Matthews, and T. W. Hyde, Phys. Rev. E 90, 033101 (2014).

[50] K.B. Chai and P. M. Bellan, Astrophys. J. 802, 2, 112 (2015).

[51] K.B. Chai and P. M. Bellan, Geophys. Res. Lett. 40, 23, 6258 (2013).

[52] J. R. Marshall, T. B. Sauke, and J. N. Cuzzi, Geophys. Res. Lett. 32,L11202 (2005).

[53] J. van eymeren and G. Wurm, Mon. Not. R. Astron. Soc. 420:183186 (2012).

[54] U. Konopka, G. Morfill, and L. Ratke, Phys. Rev. Lett. 84:891-894, 2000.

[55] A. Chokshi, A. G. G. M. Tielens, and D. Hollenbach, ApJ. 407, 806 (1993).

[56] C. W. Ormel, D. Paszum, C. Dominik, and A. G. G. M. Tielens, Astronomy and Astrophysics. 502, 845 (2009).

[57] D. A. Mendis, H. L. F. Houpis, and J. R. Hill, J. Geophys. Res. 87, 3449 (1982).

[58] D. A. Mendis, J. R. Hill, and H. L. F. Houpis, J. Geophys. Res. 88, 929 (1983).

[59] B. Walch, M. Horanyi, and S. Robertson, IEEE Trans. Plasma Sci. 22, 97 (1994).

[60] A. Barkan, N. D'Angelo, and R. L. Merlino, Phys. Rev. Lett. 73, 3093 (1994).

[61] U. Mohideen, H. U. Rahman, M. A. Smith, M. Rosenberg, and D. A. Mendis, Phys. Rev. Lett. 81, 349 (1998).

[62] M. Harwit, Astrophysical Concepts, (Springer- Verlag, New York) P. 405 (1988).

[63] J. M. Greenberg and J. I. Hage, ApJ. 361, 260 (1990).

[64] R. Wiese, V. Sushkov, H. Kersten, V. R. Ikkurthi, R. Schneider, and R. Hippler, New J. Phys. 12, 033036 (2010).

[65] M. Ilgner, A&A, 538:A124 (2012).

[66] S. Okuzumi, H. Tanaka, T. Takeuchi, and M. Sakagami, ApJ. 731, 96 (2011).

[67] Q. Ma, L. S. Matthews, V. Land, and T. Hyde, ApJ. 763, 77 (2013).

[68] P. Bagga, J. Abrahamson, and J. Marshall, Advanced Powder Technology 20, 234 (2009).

[69] L. S. Matthews, V. Land, and T. W. Hyde, ApJ. 744, 8 (2012).

[70] L. S. Matthews, R. L. Hayes, M. S. Freed, and T. Hyde, IEEE Trans. Plasma. Sci. 35, 260 (2007).

[71] C. Du, H. M. Thomas, A. V. Ivlev, U. Konopka, and G. E. Morfil, Phys. Plasmas 17, 113710 (2010).

[72] S. Khrapak and G. Morfill, Contrib. Plasma Phys. 49, 148 (2009).

[73] J. Kong, T. W. Hyde, B. Harris, K. Qiao, and J. C. Reyes, IEEE Trans. Plasma Sci. 37, 1620 (2009).

[74] K. U. Riemann, J. Phys. D: Appl. Phys. 24, 493 (1991).

[75] Z. Zhang, K. Qiao, J. Kong, L. Matthews, and T. Hyde, Phys. Rev. E 82, 036401 (2010).

[76] S. V. Vladimirov and M. Nambu, Phys. Rev. E 52 R2172 (1995).

[77] T. W. Hyde, J. Kong, and L. S. Matthews, Phys. Rev. E. 87, 053106 (2013).

[78] http://rsbweb.nih.gov/ij/

[79] A. Douglass, V. Land, K. Qiao, L. S. Matthews, and T. Hyde, Phys. Plasmas 19, 013707 (2012).

[80] Z. Zhang, K. Qiao, J. Kong, L. Matthews, and T. Hyde, Phys. Rev. E. 82, 036401 (2010).

[81] J. H. Chu and Lin I, Phys. Rev. Lett. 72, 4009 (1994).

[82] A. Melzer, T. Trottenberg, and A. Piel, Phys. Lett. A 191, 301 (1994).

[83] A. Melzer, V. A. Schweigert, and A. Piel1, Phys. Rev. Lett. 83, 3194 (1999).

[84] A. Melzer, V. A. Schweigert, I. V. Schweigert, A. Homann, S. Peters, and A. Piel, Phys. Rev. E 54, 46 (1996).

[85] J. Kong, K. Qiao, L. S. Matthews, and T. W. Hyde, Phys. Rev. E 90, 013107 (2014).

[86] J. Kong, T. W. Hyde, L. S. Matthews, K. Qiao, Z. Zhang, and A. Douglass, Phys. Rev. E 84, 016411 (2011).

[87] K. Takahashi, T. Oishi, K. Shimomai, Y. Hayashi, and S. Nishino, Phys. Rev. E 58, 7805 (1998).

[88] V. Vyas, and M. J. Kushner, J. Appl. Phys. 97, 043303 (2005).

[89] W. J. Miloch, M. Kroll, and D. Block, Phys. Plasmas 17, 103703 (2010).

[90] M. Lampe1, G. Joyce1, G. Ganguli1, and V. Gavrishchaka, Phys. Plasmas 7, 3851 (2000).

[91] G. A. Hebner, M. E. Riley, and B. M. Marder, Phys. Rev. E 68, 016403 (2003).

[92] A. Melzer, V. A. Schweigert, and A. Piel, Phys. Scr. 61, 494 (2000).

[93] V. A. Schweigert et al., Phys. Rev. E 54, 4155 (1996).

[94] D. He, B. Ai, H. K. Chan, and B. Hu, Phys. Rev. E 81, 041131 (2010).

[95] G. A. Hebner et al., Phys. Rev. Lett. 87, 2350011 (2001).

[96] U. Konopka, G. E. Morfill, and L. Ratke, Phys. Rev. Lett. 84, 891 (2000).

[97] J.Carstensen, F. Greiner, D. Block, J. Schablinski,W. J. Miloch, and A. Piel, Phys. Plasmas 19, 033702 (2012).

[98] M. Lampe, G. Joyce, and G. Ganguli, IEEE Trans. Plasma Sci. 33, 57 (2005).

[99] V. N. Tsytovich, Y. K. Khodataev, R. Bingham, Comments Plasma Phys. Control. Fusion 17, 249 (1996).

[100] S. Hamaguchi, Comments Plasma Phys. Control. Fusion 18, 95 (1997).

[101] A. Douglass, V. Land, K. Qiao, L. S. Matthews, and T. Hyde, Phys. Plasmas 19, 013707 (2012).

[102] J. Harry, Introduction to Plasma Technology. Wiley-VCH (2010).

[103] Y. Qizheng and T. Dan, J. Phys. D: Appl. Phys. 40, 4836 (2007).

[104] J. R. Marshall, T. B. Sauke, and J. N. Cuzzi, Geophysical Research Lett. 32, L11202 (2005).

[105] J. E. Daugherty, R. K. Porteous, and D. B. Gravesa, ApJ. 73, 4 (1993).

[106] G. Lapenta, Phys. Rev. Lett. 75, 24 (1995).

[107] S. V. Vladimirov, S. A. Maiorov, and N. F. Cramer, Phys. Rev. E 67, 016407 (2003).